COMPARISON BETWEEN PARTICLE IMAGE VELOCIMETRY AND LASER DOPPLER VELOCIMETRY MEASUREMENTS INSIDE THE TAMU REACTOR CAVITY COOLING SYSTEM EXPERIMENTAL TEST FACILITY

A Thesis

by

JOHN LAYNE BUDD

Submitted to the Office of Graduate and Professional Studies of
Texas A&M University
in partial fulfillment of the requirements for the degree of

MASTER OF SCIENCE

Chair of Committee,	Yassin A. Hassan
Committee Members,	William H. Marlow
	Maria D. King
Head of Department,	Andreas A. Polycarpou

May 2016

Major Subject: Mechanical Engineering

ABSTRACT

To further efforts for studying the TAMU air-cooled Reactor Cavity Cooling System (RCCS) experimental test facility, Laser Doppler Velocimetry (LDV) experiments have been conducted to acquire data on the instantaneous streamwise and spanwise components of velocity at various locations inside the upper plenum. These experiments were performed under steady-state conditions, both heated and adiabatic, using four active risers. The apparatus used for data acquisition consisted primarily of a 2-D laser head mounted onto a 3-D traverse system. Olive oil particles with an average diameter of 0.745 μm were utilized for seeding the flow.

The data from these experiments has been necessary for characterizing the experimental facility by verifying the system's repeatability and performance. In addition, LDV measurements have provided means of comparison for previously acquired PIV measurements. The compared parameters include the streamwise velocity component, as well as the streamwise and spanwise components of the turbulent intensity and the Reynolds stresses.

Based on these comparisons, several differences were found between the two techniques. First, the PIV turbulent statistics did not generally agree well with those of the LDV measurements. However, data points located at regions of higher elevation tended to have better agreement. These higher regions are characterized by velocity gradients significantly smaller than those found at lower elevations. This fact may aid in explaining the discrepancies between the techniques, since PIV is known to underperform on regions with high velocity gradients. In addition, it is suspected that the number of samples for

PIV, 150 in total, were insufficient for obtaining reasonable statistics. This is in contrast to LDV, which had 1500 samples per data point. Second, the comparison between the techniques appear to agree better for the adiabatic case than the heated case. Since the heated case has additional turbulence fluctuations induced by thermal mixing, this may have hindered the PIV measurements. Third, the turbulence intensities were consistently overestimated by PIV. This led to the conclusion that the PIV data contained significantly more noise than LDV data.

Aside from comparisons between the two techniques, several experiments were conducted to test the repeatability and accuracy of the LDV measurements. It was found that the LDV measurements exhibited good accuracy and a high level of repeatability. Throughout these measurements, the standard deviation percentage was found to be no greater than 10%. More importantly, when averaging the values of all data points at each respective each elevation, the average value ranged between 2.2% and 3.5%.

TABLE OF CONTENTS

LIST OF FIGURES

Page

LIST OF TABLES

Page

1. INTRODUCTION

A popular area of research for the nuclear power industry lies in developing fully passive decay heat removal systems, which have also become a primary focus in the development of advanced reactor designs. These systems are designed to act as ultimate heat sinks, through which the decay power from their corresponding reactors may be removed under off-normal circumstances (Figure 1). Removing the decay power from the reactor effectively limits the fuel and associated components' temperatures from extending into hazardous, unsafe levels and obviates the possibility of a reactor core meltdown.

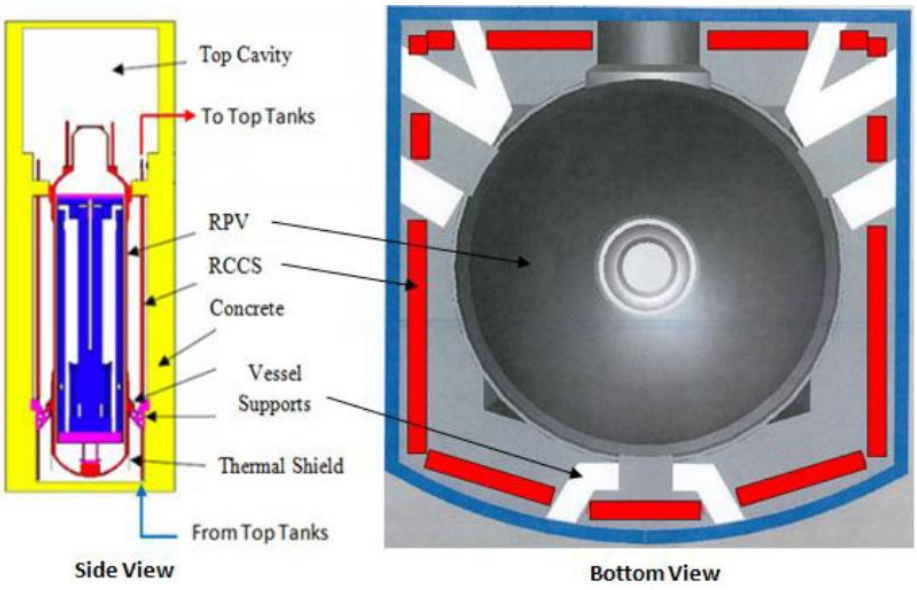

Figure 1. Schematic for a typical RCCS configuration.

A highly desirable attribute for many of these systems' designs is that they be fully passive, in which they able are operate reliably, independent of active systems and human operators, for a time period of days. To this end, natural circulation air loops have the ability to meet these needs due to the abundance of ambient air and their intrinsic safety features. Because of these and other factors, a type of passive safety system known as the reactor cavity cooling system (RCCS) has become a prime candidate for use in the Next Generation Nuclear Plant (NGNP) gas-cooled thermal reactor design, and particularly the Very High Temperature Gas-Cooled Reactor (VHTR). The VHTR concept was classified in the Generation IV technology roadmap (U.S. DOE Nuclear Energy Research Advisory Committee (NERAC) and the Generation IV International Forum, 2002; Office of Advanced Nuclear Research, DOE Office of Nuclear Energy, Science, and Technology, U.S. DOE, 2005) as one of the candidates for the NGNP, and is loosely defined as any reactor design with a coolant outlet temperature of 1000 $^{\circ}$C or above (Chapin et al., 2004).

Passive decay heat removal systems have been around as early as the 1950s, primarily used for high temperature gas reactor (HTGR) designs. RCCS designs which are either water-cooled or air-cooled have been considered (**Error! Reference source not found.**). Some, such as the Japanese high temperature engineering test reactor (HTTR), employ an RCCS which is driven via water forced convection and utilizes a set of water stand pipes and radial fins. Though this RCCS is not considered fully passive, other designs, such as those for the Chinese high temperature reactor (HTR-10) or the South African pebble bed modular reactor (PBMR), use water natural convection loops which are themselves cooled by the natural convection of air. Still others, such as those for the

Russian gas turbine modular helium reactor (GT-MHR) and the American modular high temperature gas-cooled reactor (MHTGR), are cooled entirely by the natural convection of air. Though these designs differ between nations, they all serve the primary purpose of safeguarding their respective reactors in the event of accident scenarios.

Table 1. Properties of several HTGRs and their respective RCCSs (Park et al., 2006; Corradini et al., 2012).

Country	Reactor	Power (MWt)	RCCS Coolant /Type	Secondary Coolant / Type
Japan	HTTR	30	Water Forced Convection	Water Forced Convection
China	HTR-10	10	Water Natural Convection	Air Natural Convection
South Africa	PBMR	400	Water Natural Convection	Air Natural Convection
Russia	GT-MHR	600	Air Natural Convection	No Secondary Cooling
USA	MHTGR	450	Air Natural Convection	No Secondary Cooling

As stated before, fully passive decay heat removal systems offer the means to effectively remove decay heat from the surface of the reactor pressure vessel (RPV) without the use of active systems, backup power supplies, or human intervention. Though the idea of passive systems has been around for decades, they are not currently employed in most operating power plants, which instead use active cooling via pumps powered by

off-site sources. However, this trend is poised to change as newer Generation IV reactor designs such as the VHTR are eventually constructed. For the VHTR, the RCCS provides an avenue to remove decay heat from the reactor core via reactor pressure vessel during accident events. However, due to the inherent complexities associated with natural convection systems in general, much interest has been generated with regards to understanding the characteristics such a system would possess. This necessitates thorough and full-fledged investigations to comprehend all thermal hydraulic behavior, which may include flow instabilities and thermal stratification.

One particular VHTR design has been chosen by a collaboration between several research institutions in order to commence investigations. This design, which was chosen for its extensive write-up, is the General Atomics Modular High Temperature Gas-Cooled Reactor (GA-MHTGR) (Figure 2). The reactor is designed to operate at a power level of 450 MWt and would utilize coated fuel particles arranged into graphite spheres, assembled either in hexagonal fuel assemblies or placed in a critical configuration inside of an annular core (Ball, 2005). During normal operations, helium would be circulated through the coolant channels in the graphite core to remove heat before being redirected to the power conversion system (PCS). In the event of an anomalous incident, heat could be removed by means of the primary heat transfer system or the emergency shutdown cooling system (SCS) that would utilize a separate heat transfer system to remove energy from the active core. However, both of these systems would rely on electrical power to operate, and in the case of a beyond design basis accident such as a loss of off-site power, the reactor temperature would be maintained by a radial conduction path through the reactor pressure

vessel (RPV) to an annular cavity known as the reactor cavity, which is formed by the region between the RPV and reactor containment building (Chapin et al., 2004). Heat transferred to this region could then be removed by way of the RCCS to an ultimate heat sink, the atmosphere.

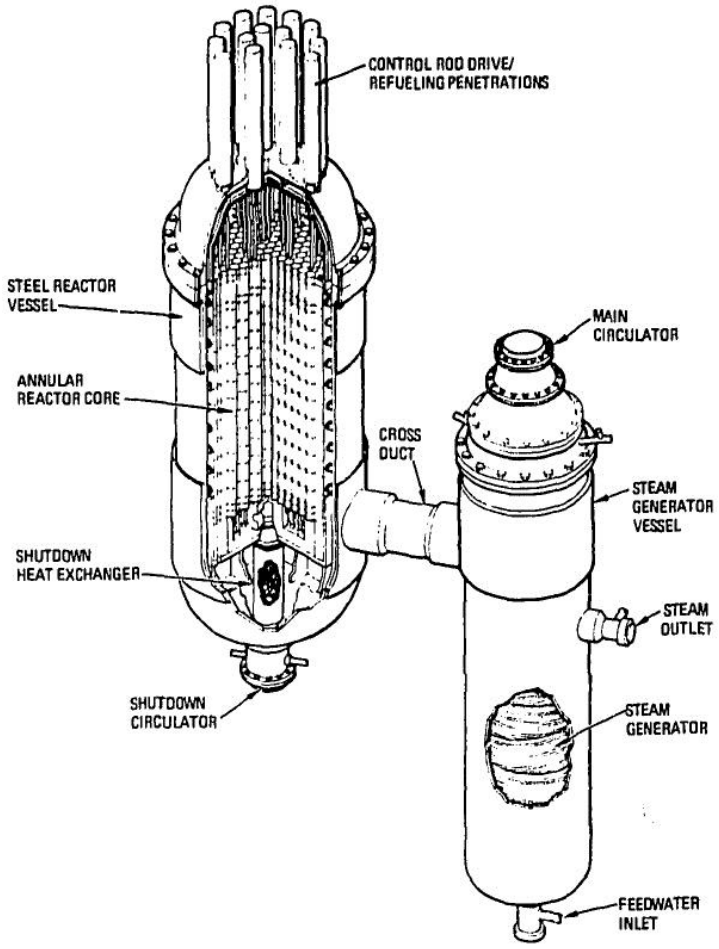

Figure 2. Schematic for the GA-MHTGR (HTGR-86-024).

There are currently two variations of the RCCS for the MHTGR design under consideration, one which is water-cooled and the other which is air-cooled. The water-cooled RCCS uses natural convection to remove heat through a natural circulation closed loop, rejecting heat from the RPV by a series of water tubes, cooling panels, and water storage tanks (Corradini et al., 2012). The other form uses an open loop configuration, which is driven by natural convection of air as the primary means of passive heat removal. Heat is transferred from the RPV through radiation and convection to a set of cooling panels and air-ducts on the wall of the reactor containment building. Both water and air have been proposed for the RCCS and are designed to operate in passive-mode, providing for long-term cooling of the RPV for both normal and accident operations (Corradini et al., 2012).

The proposed air-cooled RCCS consists of a series of air ducts that follows the interior outline of the reactor cavity walls, 227 units in total, each having a rectangular cross sectional area of 5 cm x 25 cm (2” x 10”) with a total length of 19.2 m (HTGR-86-024, 1992) (Figures 3 and 4). The planned total elevation right from the chimney inlet to the bottom of the air duct is over 55m. (Corradini et al, 2012). The system is driven by decay heat given off by the surface of RPV in the form of convection and thermal radiation. During operation, the RPV heats the surface of the risers, which in turn heats the air inside the risers. This creates a buoyancy force, which drives ambient air through the cold plenums and the downcomers, and simultaneously forces the heated air from the risers, through the hot plenums and eventually through the chimneys, after which it is vented to the atmosphere. Given the abundance of atmospheric air and the lack of active

systems, this particular RCCS would be able operate indefinitely with minimal maintenance and a high level of reliability.

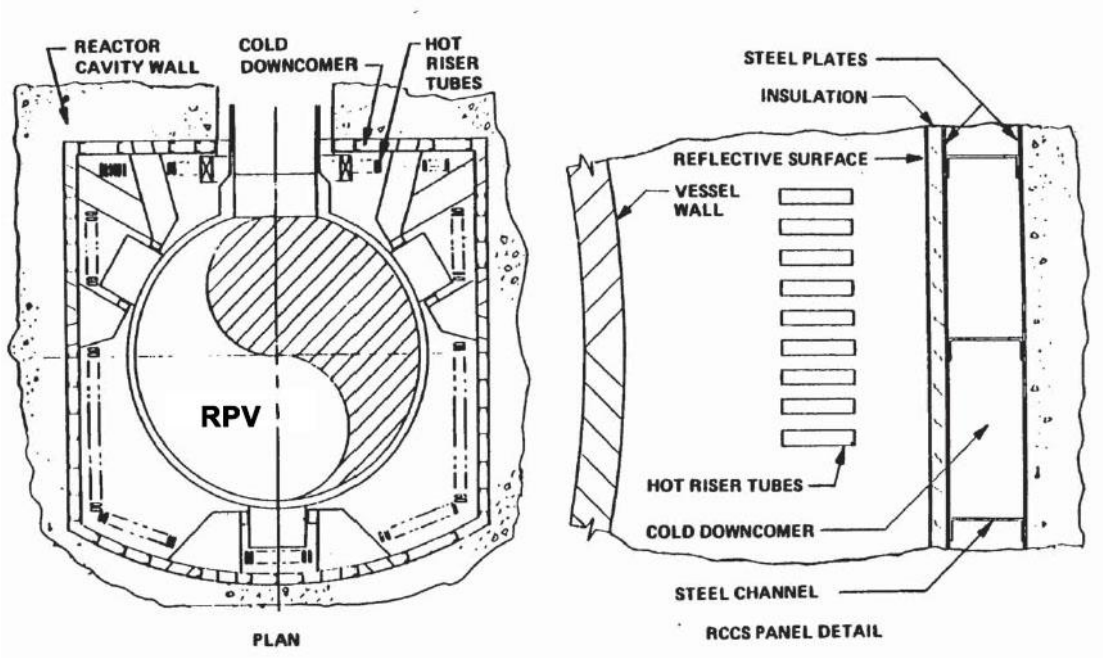

Figure 2. The RCCS cooling panel layout as envisioned for the GA-MHTGR (HTGR-86-024, 1992).

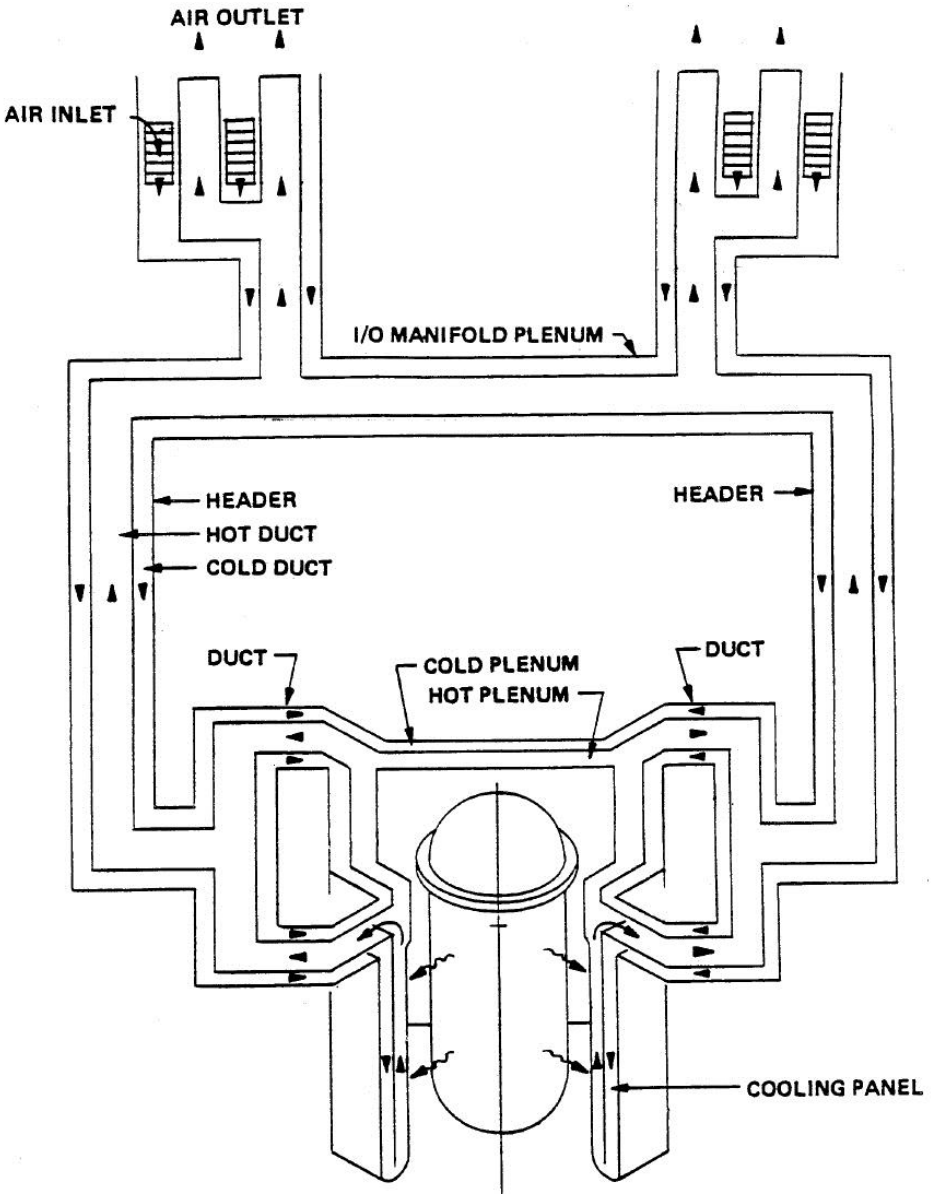

Figure 4. The RCCS duct system for the GA-MHTGR (Konefal et al., 2009).

A collaboration between Texas A&M University (TAMU), the University of Wisconsin-Madison (UW-Madison), and Argonne National Laboratory (ANL) has been created to investigate the thermal-hydraulic characteristics of the air-cooled RCCS. The primary objective of this collaboration has been the compilation and extensive study of a set of experimental data that could be implemented in computational fluid dynamics (CFD) or thermal-hydraulics codes, which ultimately should aid in predicting the prototype's actual performance. To this end, scaled experimental facilities at each location were constructed based on the prototype. The facility located at ANL is 1/2 scale of the prototype and uses radiant heaters to simulate the surface of the RPV. The facility at UW-Madison is 1/4 scale and also uses radiant heaters to drive the natural convection in the system. The facility at TAMU is 1/8 scale of the prototype. However, unlike the other collaborators, the TAMU air-cooled RCCS is driven by forced convection instead of natural convection in order to grant flexibility for establishing the upper plenum inlet boundary conditions. Since the primary purpose of the facility is to gather complementary data on the upper plenum and chimney exhausts, the use of forced convection over natural convection is justified. Also in contrast to the other collaborators, the TAMU facility is located inside an environmentally-controlled building which minimizes any atmospheric interference with the facility's operation (Sulaiman, 2015).

Since its completion in early 2014, a wide range of experiments have been conducted to study pertinent multifaceted thermal hydraulic phenomena inside the TAMU air-cooled RCCS, particularly inside the upper plenum. These experiments have gathered data in the form of 2-d temperature and velocity profiles, which have been collected using

moveable thermocouple racks and Particle Image Velocimetry (PIV), respectively. Based on the results of several cases, it was evident that either thermal stratification or flow reversal (or both) could occur inside the upper plenum. The onset of either phenomena would be highly detrimental for the successful operation of the prototype, each of which would act to inhibit the mixing inside the upper plenum and reduce the overall heat removal efficiency of the system. Though there is uncertainty as to precisely which mechanisms trigger these phenomena, the phenomena themselves are known to be highly sensitive to the boundary conditions.

In order to further study these peculiarities inside the upper plenum, LDV experiments are actively being conducted. The following are the objectives of the LDV experiments, which serve as the scope for this work: 1) Collect data to perform comparisons between the PIV and LDV measurements for the streamwise component of mean velocity, the streamwise and spanwise components turbulent intensity, and the Reynolds stress, and 2) conduct experiments which will verify the system's stability and the repeatability of measurements.

Objective 1) is the primary objective of the experiments, in which PIV data of lower statistics (150 samples) is compared to LDV of higher statistics (1500 samples). So far the comparisons have yielded considerable insight, with several similarities and a few key discrepancies found. This comparison includes the standard errors related to both techniques. The purpose of objective 2) is to provide data which verified the stability of the system under steady state conditions, for both adiabatic and heated conditions. These experiments consist of taking repeated measurements at several locations and calculating

the standard deviation of the measurements at each location. They are designed to detect any long-term transients in the system which are not easily detectable by PIV measurements, which are taken over the course of an hour instead of many hours.

2. LITERATURE REVIEW

Due to the limitations of theoretical analysis and computation fluid dynamics (CFD) in describing the complex nature of turbulent flows, experimental investigations have long been and will continue to be vital for understanding the behavior of these flow regimes. To this end, devices such as hot wire anemometers and Pilot tubes have been traditionally used for measuring turbulence parameters. For Pilot tubes, it is difficult to calculate the velocity fluctuations from the resulting pressure data due to low response times. In this sense, hot wire anemometers are superior to Pilot tubes in that they have a rapid response to local velocity changes, and thus can measure velocity fluctuations accurately. Due partially to this attribute, hot wire anemometers have been widely used tools for velocity measurements. However, they are limited from making measurements in high velocity water flows and flows containing hard particles, and usually need be calibrated before each use. Moreover, both of these devices suffer from needing to be inserted directly into the flow. This insertion causes flow disturbances, and in the case of hot wire anemometers can cause blockage for pipes and ducts of small cross-sectional area. In addition, this prohibits either device from being used in extreme environments, or in regions where mechanical access is not possible (Zhang, 2010).

These are among the reasons which have led to the development of different types of velocity measurement techniques, a sizeable portion of which involve using light sources and detectors. One such technique which has become prominent in experimental fluid mechanics is Laser Doppler Velocimetry (LDV), or Laser Doppler Anemometry

(LDA). LDV refers to an optical method for locally measuring one or more components of instantaneous velocity. It falls under the class of interferometry, a category of techniques which utilize interference patterns created by mutually coherent light waves. In application to fluid mechanics, these interference patterns are used to measure the local flow velocity by calculating the time a tracer particle takes to traverse one or more of fringes, known as transit time. For LDV, intensity variations produced by particles moving through an interference pattern are reflected and Doppler-shifted, which are measured by a photo detector and converted into electric signals. These signals yield information about particle velocity and position relative to the laser and the detector (Durst et al., 1981). Provided that the particle accurately follows the flow, the particle velocity is close to the flow velocity. If this is not the case and there exists a slip velocity, it must be known to accurately measure the flow (Albrecht et al., 2003).

There are several inherit properties of LDV which make it attractive for measurements. First and foremost, because it is an optical technique, there is no need for any insertion into the flow. This means it may be used without requiring physical access and may be used in extreme environments. This is true provided there are adequate seeds supplied to the flow and there is an optically transparent surface for the laser to travel through. Second, LDV systems are highly directionally dependent, in that the measuring direction is defined solely by the orientation of the system and is truly cosine in response. Third, due to the stability and linearity of electromagnetic waves, no calibration of the probe is required. Aside from this, there are two additional advantages, in that it leads to measurements being independent of parameters such as pressure and temperature, and the

response of LDV is absolutely linear. Fourth, LDV data has high spatial and temporal resolution. This makes it ideal for point velocity measurements and for analyzing turbulent statistics, the temporal resolution of which is usually limited by seeding characteristics and not by the equipment. Finally, LDV systems may be used for measuring multiple components of velocity at the same point, which is achieved by using multiple laser s with different wavelengths. It is also capable of detecting reverse flow velocities by using a Bragg Cell to shift one of the lasers' frequencies (Dantec Dynamics, 2011). These properties have catalyzed the development of LDV, which has progressed greatly over several decades (Zhang, Albrecht, Durst).

The conceptual principle LDV was first introduced by Yeh and Cummins (Yeh and Cummins, 1964) in application to measuring developed laminar pipe flow (Zhang, Albrecht, Durst). Since these initial developments, LDV has steadily evolved due to rapid advances in optics and electronics technology as well as the tremendous growth of computing power. Several common arrangements have emerged, namely the "reference-beam", "dual-beam", and "two-scattered beam" modes, with the former two techniques being the most frequently used. (Durst et al, 1981)

The reference-beam mode, which was pioneered by Yeh and Cummins, utilizes a laser split into an intense scattering beam and a weaker reference beam. When light from the scattering beam hits tracer particles, it is reflected and its frequency is Doppler-shifted. This light interferes with the reference beam, which is directed onto a photocathode, and produces a frequency difference which is proportional to the particle velocity. Alternatively, the dual-beam mode was first used by Durst and Whitelaw and in contrast

involves two lasers of equal intensity. The beams are aligned to intersect and produce a measurement volume which contains an interference pattern. Particles moving though this measurement volume pass through an alternating pattern of fringes, the scattered light from which also produces a frequency difference proportional to the particles' velocity. The third technique, two-scattered beam mode, has been discussed by Mazumder and Wankum, and it utilizes a focused laser aligned into the flow. Pulses from this laser are detected from two symmetric locations about the system axis. For the light scattered off a particle, the relative phase of these wave fronts detected at each location is related to the distance from the particle. When these two signals are superimposed onto each other, the result is a signal which has a frequency equal to the Doppler frequency, proportional to the particle's velocity. Since this method offers no distinct advantages from the other two techniques and suffers from the issue of aperture broadening, the other two techniques have been more widely utilized (Durst et al, 1981). The focus of this work will be on the second technique mentioned, the dual-beam mode.

The basic principle of LDV can be visualized through Figure 5, which portrays the geometry of a basic LDV setup. The figure shows a laser emitting monochromatic light at wavelength λ_b and frequency f_b in the $\mathbf{e}_b$ direction, which is along the z-axis. A tracer particle moving at velocity $\boldsymbol{v}_p$ passes through the origin and intersects the laser. The laser light is scattered and double Doppler shifted to frequency f_r. Some of this light is received by a receiver in the $\mathbf{e}_{pr}$ direction, which is at an angle ϑ_s to the z-axis, and is converted in a signal with frequency directly related to the particle velocity. Mathematically, this relationship is represented as:

$$f_r \approx f_b + f_b \frac{\boldsymbol{v}_p \cdot (\boldsymbol{e}_{pr} - \boldsymbol{e}_b)}{c} = f_b + \frac{\boldsymbol{v}_p \cdot (\boldsymbol{e}_{pr} - \boldsymbol{e}_b)}{\lambda_b}$$

The second term in the equation is the Doppler-shifted frequency, which is proportional to the velocity component perpendicular to the laser light in the direction of the x-axis. The magnitude of this term usually ranges from 1 – 100 MHz, and is much smaller than the frequency of the incident laser light. Because of this, direct measurement of the Doppler-shift is difficult and impractical for most experiments (Albrecht et al., 2003).

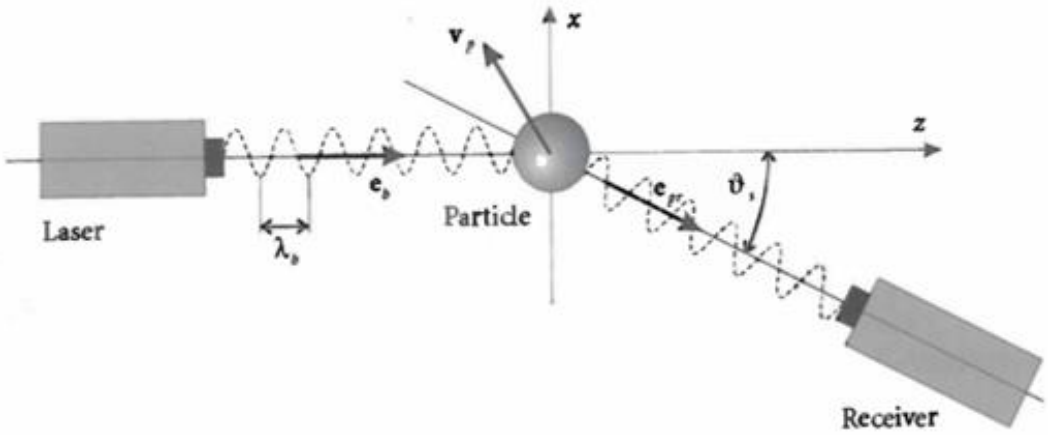

Figure 5. Basic LDV experimental setup (Albrecht et al., 2003).

A more realistic LDV setup is the dual-beam configuration, which is featured in Figure 6. Here, two lasers of wavelength λ_b and frequency f_b are set to intersect at the origin, with their orientations given by $\mathbf{e}_1$ and $\mathbf{e}_2$. A particle passes through the origin with

velocity $\mathbf{v}_p$, which scatters light from both sources. This light is Doppler shifted, some of which is received by a detector in the direction of $\mathbf{e}_{pr}$ aligned with the z-axis. The frequency of the light received from each source is given as:

$$f_1 = f_b + \frac{\boldsymbol{v}_p \cdot (\boldsymbol{e}_{pr} - \boldsymbol{e}_1)}{\lambda_b}, f_2 = f_b + \frac{\boldsymbol{v}_p \cdot (\boldsymbol{e}_{pr} - \boldsymbol{e}_2)}{\lambda_b}$$

This leads to the more significant expression for Doppler frequency:

$$f_D = \frac{\boldsymbol{v}_p \cdot (\boldsymbol{e}_1 - \boldsymbol{e}_2)}{\lambda_b}$$

There are two significant features of the previous equation. First, the Doppler frequency is independent of the detector direction. This implies the detector location does not need calibration and may be placed in any configuration, including forward scattering, back scattering, etc. In particular, the back scattering configuration can be used in modularizing commercial LDV setups, which allows them to be mounted onto traverse systems for taking measurements at many different locations. However, it should be noted that the intensity of the scattered light is highly anisotropic, which should be a consideration for experimental setups. Second, the Doppler frequency does not need to be distinguished from the incident light frequency f_b, since it is effectively "filtered out" through taking the difference of each velocity. It should also be noted that the Doppler frequency itself is inversely proportional to λ_b. This makes the Doppler frequency, and hence the particle velocity, much easier to obtain via measurements. (Albrecht et al., 2003)

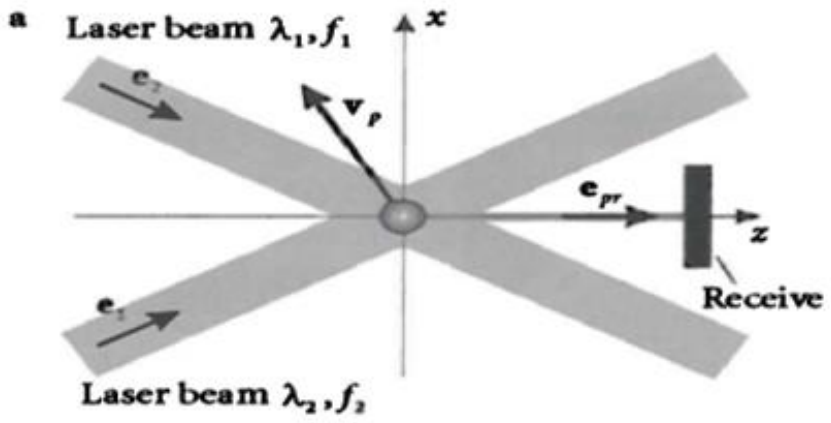

Figure 6. Dual-beam LDV experimental configuration (Albrecht et al., 2003).

With the basic idea of dual-beam LDV illustrated, a more specific topic to discuss is the measurement volume created by dual intersecting beams. Figure 7 gives a representation of this volume with relevant geometric parameters. In it, two lasers are set to intersect at the origin, with angle between them Θ. At the origin an ellipsoid-shaped volume is formed through which particles moving into it scatter light for measurements. A particle is poised to move through the volume with velocity $\mathbf{v}_p$ and angle α with respect to the x-axis. When it passes through the volume, the Doppler frequency of the scattered light is given by:

$$f_D = \frac{2\sin(\frac{\Theta}{2})}{\lambda_b}|\mathbf{v}_p|\cos\alpha = \frac{2\sin(\frac{\Theta}{2})}{\lambda_b}\mathbf{v}_{p\perp}$$

Where $|\boldsymbol{v}_p|$is the magnitude $\mathbf{v}_p$ and $\boldsymbol{v}_{p\perp}$ is the component of velocity in the x-direction. (Albrecht et al., 2003) Though a useful illustrative model, it is also necessary to talk about the fringe patterns of the measurement volume; Figure 8 is a conceptual

example of a measurement volume constructed from these fringe patterns. In it, two monochromatic light waves of wave vectors $\mathbf{k}_a$ and $\mathbf{k}_b$ wave amplitudes E_a and E_b, intersect at the origin at an incident angle α relative to the z-axis (Note: $\alpha = \frac{\Theta}{2}$ from the previous equation). The superposition of these waves creates a region of interference patterns, or the measurement volume, and is mathematically given as:

$$E = E_a + E_b = 2E_0 \cos(kx \cdot \sin\alpha) \cdot \cos(\omega t - kz \cdot \cos\alpha)$$

Where E_0 is the amplitude of the wave amplitude and k is the amplitude of the wave vector. A more useful quantity to examine is the light intensity, given as:

$$E_m^2 = 2E_0^2 \left[1 + \cos 2\pi \left(\frac{2\sin\alpha}{\lambda_0} x\right)\right] = 2E_0^2[1 + \cos\left(2\pi \frac{x}{\Delta x}\right)]$$

Where E_m^2 is the light intensity, E_0^2 is the amplitude of the light intensity, λ_0 is the incident light wavelength, and Δx is a quantity termed the fringe spacing. The previous equation implies:

$$\Delta x = \frac{\lambda_0}{2\sin\alpha}$$

The fringe spacing is a physical and geometric constant determined solely by the parameters of the LDA setup and the indices of refraction for the experiment itself. This ultimately means the system does not require calibration aside from the lasers' wavelength and incident angle, which for commercial setups is typically controlled to a high degree. It is the distance between adjacent fringes in the direction of the x-axis, and so applies to measurements of the component of velocity in this direction. For measuring this component of velocity, given a particle with velocity $\mathbf{u}_p$:

$$u_\perp = \Delta x \cdot \nu_D$$

Where $u_{\perp}$ is the velocity component in the x-direction and ν_D is the Doppler frequency. From this equation, one can interpret the Doppler frequency as the frequency of the intensity of scattered light from the particle, the shape of which is shown in Figure 8. This signal is known as a Doppler burst, and is plotted on an intensity versus time graph. It features a peak intensity at the center of the pulse which corresponds to the particle being located nearest to the center of the measurement volume. The pulse also tails off on either side, which corresponds to the particle being furthest from the center of the volume. The reason for the spatial dependence of the intensity is due to the Gaussian profile of each laser, which has a peak in the center and tails off towards the edges. (Zhang, 2010)

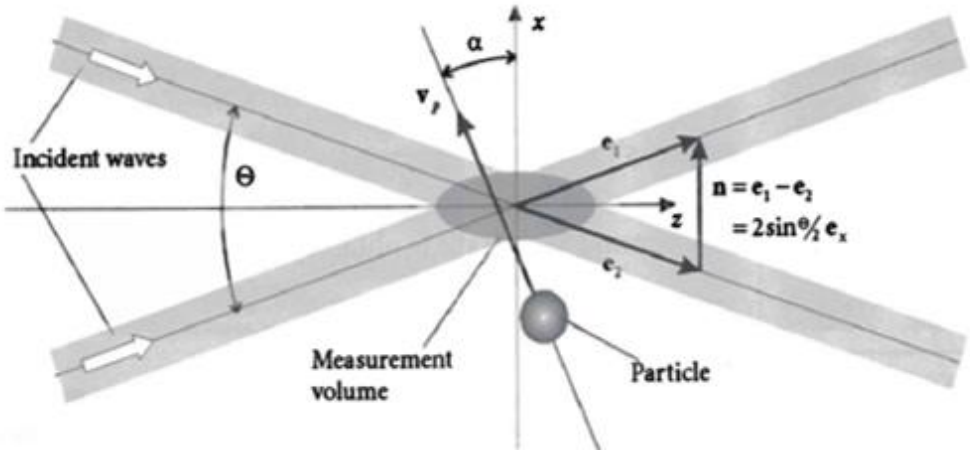

Figure 7. Measurement volume for LDV measurements (Zhang, 2010).

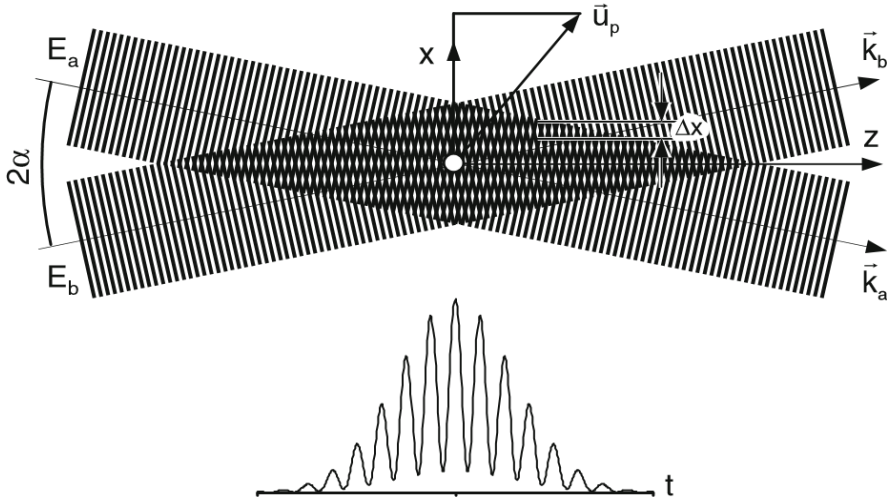

Figure 8. Conceptual diagram for visualizing the fringe nature of the measurement volume (top) and a typical "burst" or measurement pulse (bottom) (Zhang, 2010).

A final topic to discuss is that of resolving the flow direction for LDA measurements. Since the Doppler frequency is always positive, this only allows for the measurement of the particle speed and not its direction. To rectify this, a Bragg cell is commonly employed to create a frequency shift for one of the lasers. Bragg cells are devices which use fluctuating pressure waves generated by acoustic transducers to create a sinusoidal phase grating in a crystal. This phase grating increases the frequency of any light waves passing through it by a precisely controlled amount (Albrecht et al., 2003). This frequency shift is usually on the order of tens of megahertz, which is much lower than the incident light frequency but higher than the Doppler frequency. Analytically, this frequency shift is incorporated into the equation as:

$$u_{\perp} = \Delta x \cdot (\nu_{PM} - \nu_{sh})$$

Where ν_{PM} is the effective frequency measured by the photomultiplier and ν_{sh} is the shift frequency. With the shift frequency precisely known, the velocity can also be determined by measuring ν_{PM}. The value of ν_{PM} may be greater than, less than, or equal to the shift frequency, which depends of course on the particle velocity. When the laser with shifted frequency interacts with the laser without shifted frequency, the resulting measurement volume has an unsteady fringe pattern which "rolls" in the x-direction (Figure 9). The velocity of this fringe motion relative to the measurement volume is given by:

$$u_{sh} = \frac{dx}{dt} = -\nu_{sh}\Delta x$$

Where u_{sh} is the fringe velocity. One can interpret the fringe velocity such that, when a particle has zero velocity relative to the motion, the value for ν_{PM} is equal to the shift frequency ν_{sh} and the velocity component $u_{\perp}$ is zero (Zhang, 2010).

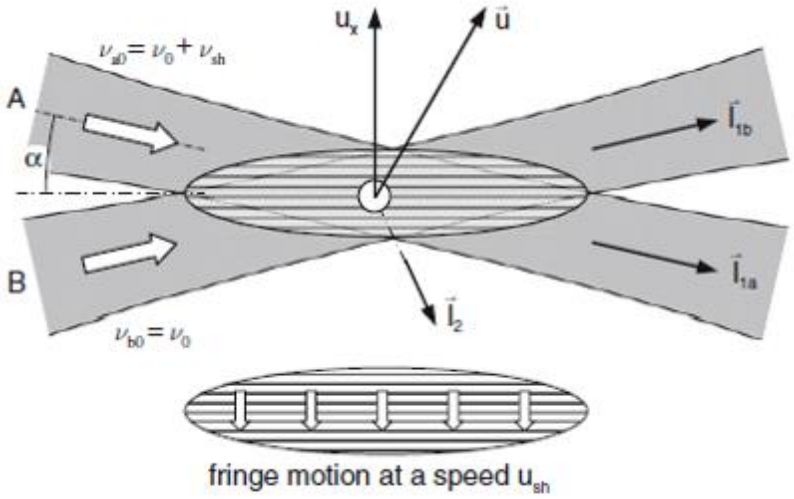

Figure 9. Fringe motion inside the measurement volume created by the interaction of two lasers at different frequencies (Zhang, 2010).

3. FACILITY OVERVIEW

As stated previously, the TAMU air-cooled RCCS test facility was completed in early 2014 to provide complementary and CFD-grade experimental data for the collaboration. The design parameters of the facility were based on previous scaling analysis by ANL and UW-Madison (Tzanos et al., 2006). The actual design of the TAMU facility has been discussed by Sulaiman, the parameters for which are featured in Tables 2 and 3 (Sulaiman et al., 2015). The finished facility and the primary engineering schematic are featured in Figure 10 (Sulaiman, 2015).

Table 2. Key design parameters for the TAMU facility (Zhang, 2010).

Parameter	**Value**
Temperature difference, ΔT	130 ˚C
Cross-sectional area, A_{riser}^{1}	0.003 m^2
Hydraulic diameter, D_H	0.04 m
Velocity, U_{riser}^{1}	17 m/s
Mass flow rate, $\dot{m}_{ind}$	0.06 kg/s
Heater power, $\dot{Q}_{htr}$	8.5 kW
Entrance length, L_e	1.1 m

Table 3. Scaling parameters for the facilities involved in the collaboration (Sulaiman et al., 2015).

		ANL	**UW**	**TAMU**
Parameter	**Scaling Ratios**	**Values for $l_R = 0.50$**	**Values for $l_R = 0.25$**	**Values for $l_R = 0.125$**
Lateral (radial)	-	1.00	1.00	0.50
Velocity, U	$U_{oR} = {l_R}^{1/2}$	0.707	0.50	0.35
Time ratio, T_R^*	$T_R^* = \frac{l_R}{U_{oR}} = {l_R}^{1/2}$	0.707	0.50	0.35
Temperature rise, ΔT	$\Delta T_{oR} = \frac{\dot{Q}_R}{U_{oR} A_{oR}}$	1.00	1.00	1.00
Power, $\dot{Q}$	$\dot{Q}_R = U_{oR} = {l_R}^{1/2}$	0.707	0.50	0.354
Heat flux, q"	$q_R^{"} = {l_R}^{-1/2}$	1.414	2.00	2.828

Figure 10. The TAMU facility (left) and primary schematic (right) (Sulaiman, 2015).

The TAMU facility stands at a total height of 7.20 m, which is ½ scale of the UW-Madison facility. It primarily consists of ① four riser ducts, ② one upper plenum, ③ two twin exhaust chimneys, ④ four air blowers, and ⑤ four inline heaters. The structure of the facility is made of carbon steel, chosen for its durability and economy. The associated piping which connects the blowers, heaters and risers has an outer diameter of 2" (5.08 cm). The risers have rectangular cross-sections with outer dimensions of 5.03" (12.78 cm) by 1.05" (2.67 cm) and inner dimensions of 4.67" (11.86 cm) by 0.69" (1.75 cm), and length of 78.74" (200.00 cm). The upper plenum is rectangular with outer dimensions of 19" (48.26 cm) by 18" (45.72 cm) by 17" (43.18 cm). The chimney outlets each have an inner diameter of 6" (15.24 cm) (Sulaiman, 2015).

Of the previously mentioned components, the upper plenum is the focus of experiments and is considered the test section. It consists of three distinct sections featured in Figure 11: The four riser inlets (labeled 1-4 from left to right), the plenum chamber, and the two outlet exhaust pipes (labeled l and r respectively). These sections were of keen interest for the preliminary CFD analysis, the details of which are discussed by Sulaiman (Sulaiman et al., 2015). The upper plenum itself is made of carbon steel except for three glass panes, which allow for optical experiments such as PIV and LDV. In addition, these panes are removable and so provide access to the inside of the chamber, which made the installation of moveable thermocouple racks possible.

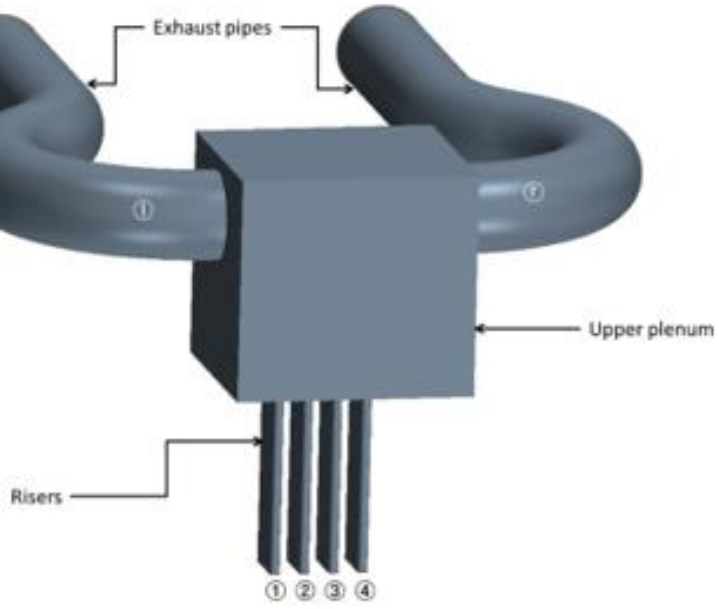

Figure 11. Test section regions of interest (Sulaiman, 2015).

The TAMU facility operates in a forced circulation, open loop fashion, which differs from the other facilities in that they operate in a natural circulation, open loop fashion. Ambient air is first drawn into the air blowers. It then proceeds to the in-line heaters which heat the incoming air to the required temperature(s). The heated air is channeled to the risers via the associated piping. The air from each riser is collected and mixed inside the upper plenum. This air eventually exits though two exhaust ducts, where it is finally released to the atmosphere.

To drive the flow, four air blowers have been installed at the bottom of the facility. Of these, two are TE5005 TISCH Environmental air blowers and two are GMB 2360 Thermo Andersen Instruments air blowers. All blowers are rated up to 8 amps (0-110 V AC) and can supply a volumetric flow rate up to 60 CFM (0.0283 m^3/s). The power to each blower is regulated by a variable autotransformer manufactured by Stacy Energy Products Company, which can be varied between 0-120 VAC and can provide up to 12 amps. Digital multimeters, model MAS830B by Commercial Electric, were used to digitize the output from each autotransformer and provide a means to monitor blower outputs. Overall, these air blowers have allowed for the stable and precise control of the upper plenum inlet velocity conditions, which are calibrated before every experiment with a TSI VelociCalc 9545-A air velocity meter (0-30 m/s, -10-60 $^{\circ}$C, ±3% of the reading or ± 0.015 m/s accuracy) (TSI, 2013).

For heating the air, four heaters were installed downstream of the blowers. These heaters are FT-400 Tutco-Farnam Custom Products open coil heaters. Each heater can supply up to 10 kW of power and can accommodate volumetric flow rates up to 500 SCFM

(0.236 m^3/s) with a maximum pressure drop of 3 psig (0.207 bar). The heaters' power are controlled by four 7550 series process controllers, which operate on separate circuits of 240 VAC and 480 VAC, and range from 0-1093 °C with 1 °C resolution. Each controller monitors the heater process temperature and the high temperature limit with two K-type thermocouple probes factory installed inside each heater. These controllers utilize PID algorithms which have been tuned specifically for the facility. This enables precise and stable control of the upper plenum inlet temperature conditions, which are monitored through several T-type thermocouple probes (8" quick disconnect, copper-constantan, exposed junction, -267 °C -260 °C, greater of 0.5 °C or 0.4% accuracy, 0.062" diameter stainless steel sheath) positioned at the centers of the inlets (Sulaiman et al., 2015).

In order to install measurement instrumentation throughout the entire facility, such as thermocouples, pressure transducers and borescopes, it was necessary to design and install instrumentation ports. Of these, the thermocouple and pressure transducer ports consist of 3/8" female NPT threaded through type fitted with 1/8" male NPT, 1/16" OD Omegalok compression fittings, which are located throughout the risers and chimney exhausts. The boroscope ports consist of 3/8" female NPT threaded through type fitted with 1/8" male NPT, 1/16" OD Omegalok compression fittings located on the risers and chimney exhausts. For the plenum specifically, several ports for pressure and temperature measurements were installed, which consist of 1/4" female NPT threaded through type fitted with steel Yor-Lok tube fitting, utilizing a straight adapter for 5/16" tube OD x 1/4" male NPT. Figures 12, 13, 14, and 15 summarize the locations of these ports throughout the facility (Sulaiman et al, 2015).

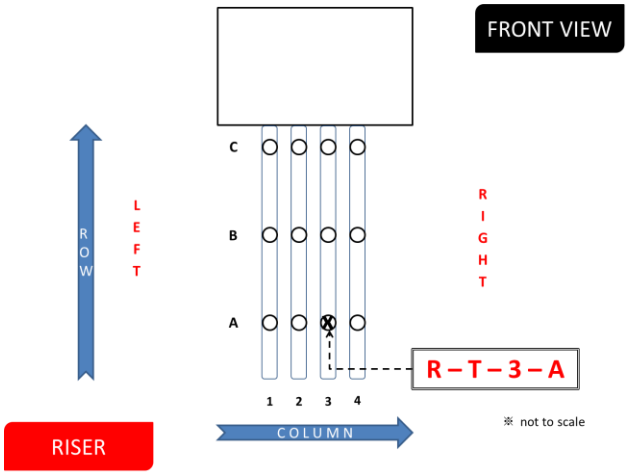

Figure 12. Riser duct instrumentation port placements (Sulaiman et al. 2015).

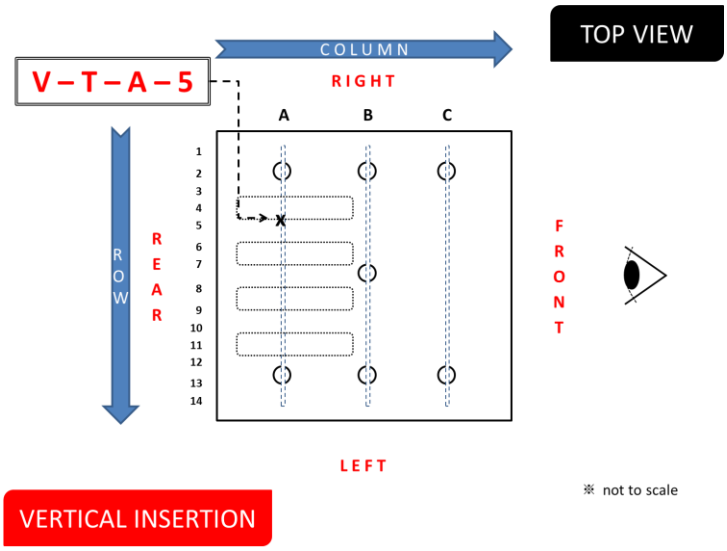

Figure 13. Upper plenum bottom plate instrumentation port and vertical thermocouple rack placements (Sulaiman et al. 2015).

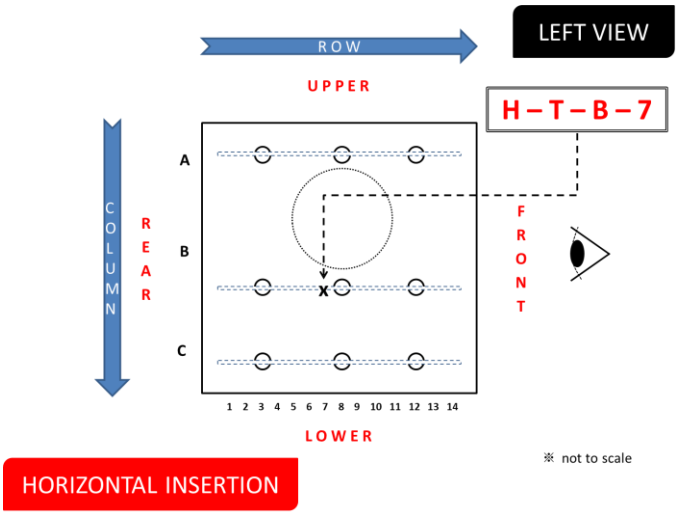

Figure 14. Upper plenum side plate instrumentation port and horizontal thermocouple rack placements (Sulaiman et al., 2015).

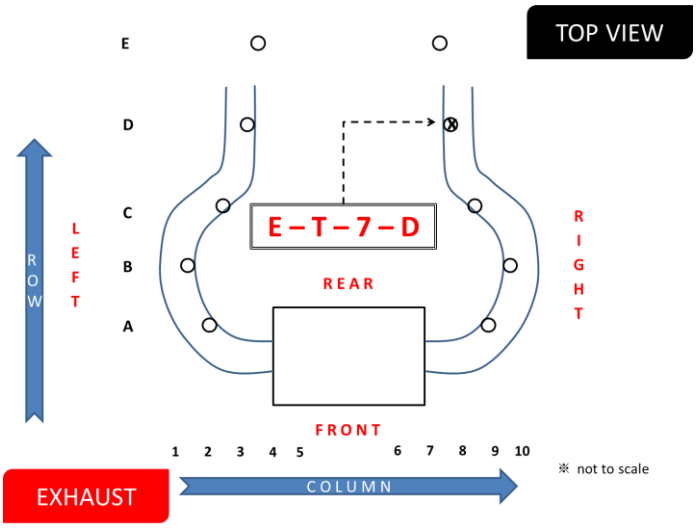

Figure 15. Chimney exhaust instrumentation port placements (Sulaiman et al., 2015).

For collecting spatial temperature profiles within the upper plenum, several thermocouple racks have been fabricated inside the upper plenum. Two sets of three racks have been made, one for vertical and one for horizontal measurements. Each rack has 14

fine wire thermocouples spaced at 1” intervals, for a total of 84 thermocouples. These racks are designated through a naming convention, with the vertical racks named VTA, VTB, and VTC, while the horizontal racks are named HTA, HTB, and HTC (Figure 16). They operate by being manually actuated to different distances inside the plenum (from 1” to 17” in 0.5” increments) via an external frame. At each distance, temperature data is recorded at a set sampling rate for set number of samples, specifically 900 samples at 90 Hz. The data is collected and interpolated to construct 3-d temperature profiles under steady-state conditions. The thermocouples used are T-type insulated fine wires (copper-constantan, -267 ^{o}C - 260 ^{o}C, greater of 0.5^{o}C or 0.4% accuracy, junction welds created by an Omega TL-welding machine). All thermocouples, including the probes, have been calibrated to within 1.5 ^{o}C using standard 2-point calibrations using both an ice bath at 0 ^{o}C and a hot bath at 100 ^{o}C, as verified by a T-type probe connected to a Fluke 52 II dual input digital thermometer (0.05% of reading + 0.3°C, type-J, K, T, E). The thermocouples are connected to the data acquisition system (DAQ), which consists of a National Instruments (NI) PXIe-1078 high performance nine-slot chassis, three NI PXIe-4353 thermocouple input modules (each has 32- channels, 24-bit analog-to-digital, high-speed (90 S/s/ch) and high-resolution (1 S/s/ch) modes), and an NI PIXe-1078 controller slot which provides control through the workstation computer. The software used for collecting data is NI Labview SignalExpress 2013 (Sulaiman, 2015).

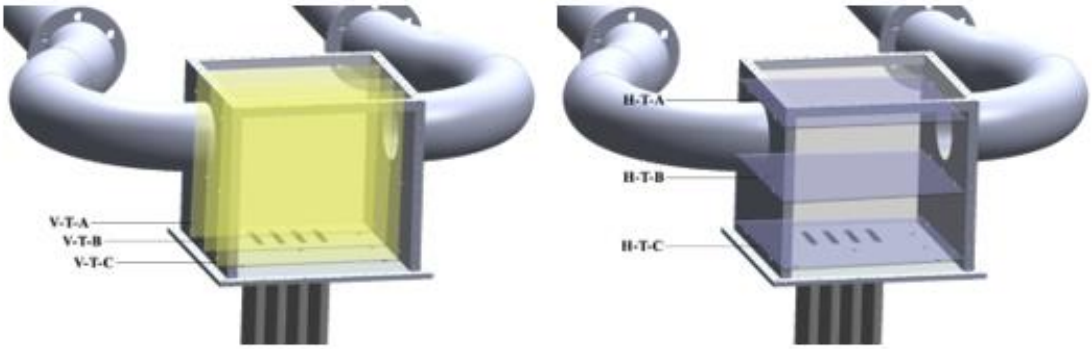

Figure 16. Vertical measurement planes VTA, VTB, and VTC (left) and horizontal measurement planes HTA, HTB, and HTC (right) (Sulaiman, 2015).

For gathering velocity data inside the upper plenum, the facility is equipped to perform either 2-D PIV or 2-D LDV. Either method requires the injection of seeding particles into the flow, which serve to reflect laser light for measurements. For the TAMU facility, olive oil droplets were selected based on several characteristics: 1) Attractive size distribution with a mean diameter of less than one micron, 2) continuous injection for several days is easily achieved, 3) olive oil is highly economical. These particles are generated with a TSI Model 9306 six-jet atomizer; the properties of these seeds are featured in Table 4. The atomizer works by using compressed air to draw olive oil from a reservoir in the form of an atomizer jet. This jet consists of liquid is broken up into large and small droplets which are carried by the compressed air. The larger droplets are bombarded onto a spherical impactor and drop back into the reservoir, though the smaller, less massive droplets are able to pass though. These smaller droplets form an aerosol which is ejected from the atomizer along with the compressed air. The resultant aerosol consists of particles with a mean diameter of 0.745 μm, which was verified under

experimental conditions using a TSI APS Model 3321 (Figure 17). The olive oil droplets are injected into the facility at the bottom of the risers, which is more than sufficient distance from the upper plenum to allow the flow to fully develop past the injection port (TSI, 2014).

Table 4. Olive oil seeding particle properties (TSI., 2014).

Description	**Specification**
Seed Material	Olive Oil
Density (kg/m^3)	0.913 g/cm^3
Refractive Index	1.47
Vapor Pressure	Very Low
Mean Particle Size (μm)	0.745 (range: 0.5 – 1.2)
Particle Output Concentration (particles/cc)	4.0×10^6

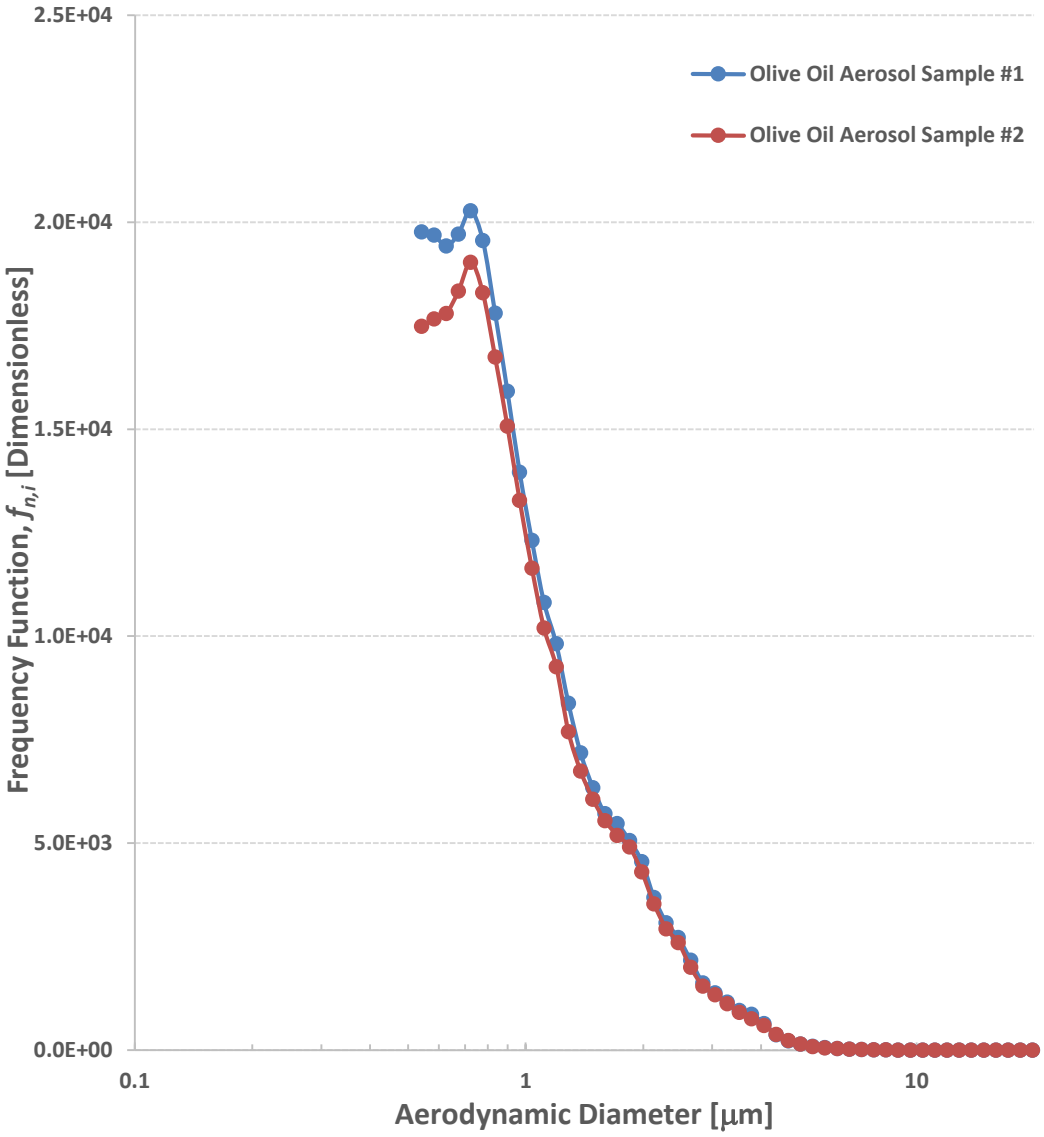

Figure 17. Seeding particle size distribution verified by an APS Model 3321 (Sulaiman, 2015).

For PIV, measurements may be taken at planes VTA-VTC, though certain modifications could allow for measurements of planes HTA-HTC. Taking PIV measurements requires the use a digital high-speed camera, a laser source, and seeding particles, the setup for which is shown in Figure 18. The digital high-speed camera which

has been used is a Phantom Miro M130. The camera is mounted onto a Dantec Dynamics 3-D traverse system which allows for fine adjustments of the position relative to the test section. The laser source is a Beamtech Vlite-200 pulsed laser, the laser arm of which is attached to a three-axis Velmex Inc. Bislide Positioning System. With the y-axis and x-axis bislides motorized (z-axis is manually controlled) and controlled by a VXM Stepping Motor Controller, aligning the laser arm with high precision is achievable (Sulaiman, 2015).

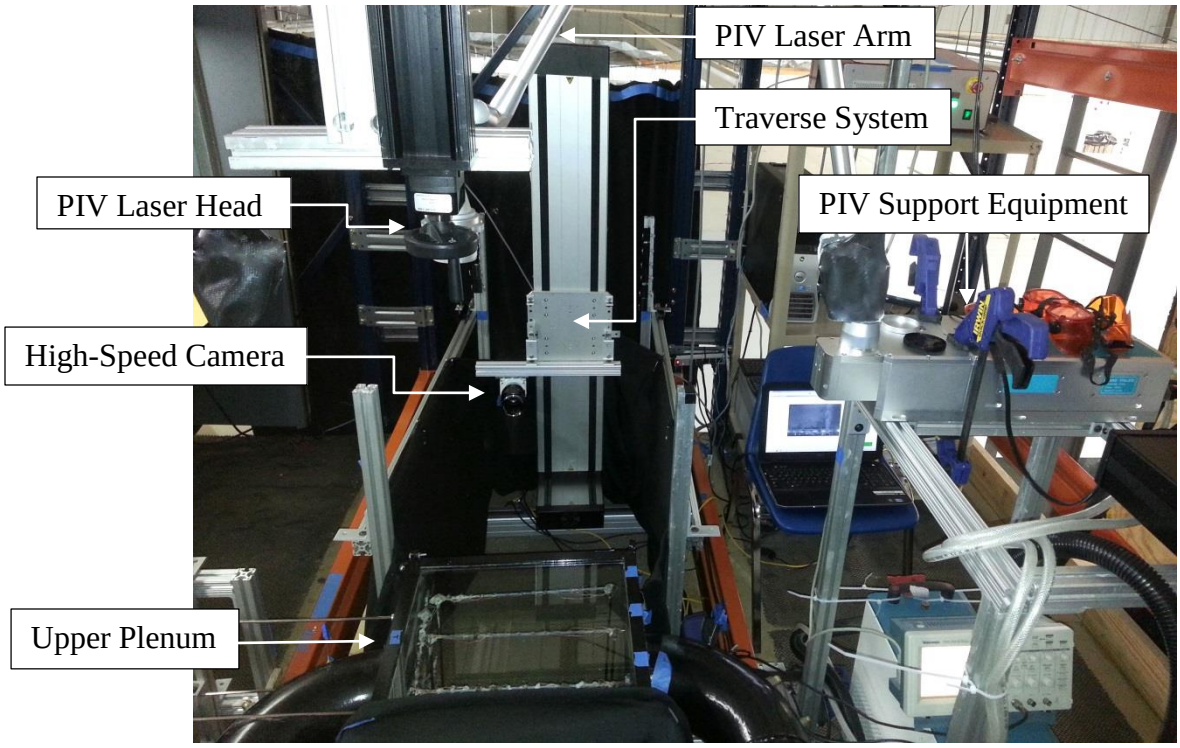

Figure 18. PIV experimental setup (Sulaiman, 2015).

4. EXPERIMENTAL SETUP

The setup for LDV similar to that of PIV, though instead of a high-speed camera and pulsed laser combination, LDV experiments only require a compact Dantec Dynamics Flow Explorer laser head. The laser head is attached to the traverse system in a fashion similar to the high-speed camera. The traverse system is designed to work in conjunction with the laser head for making pre-programmed and fully autonomous measurements at any location which is designated by the user. This allows practically endless configurations for measuring velocity profiles, provided the desired data points lie within reach of the traverse system and laser head. The experimental setup for LDV measurements is featured in Figure 19.

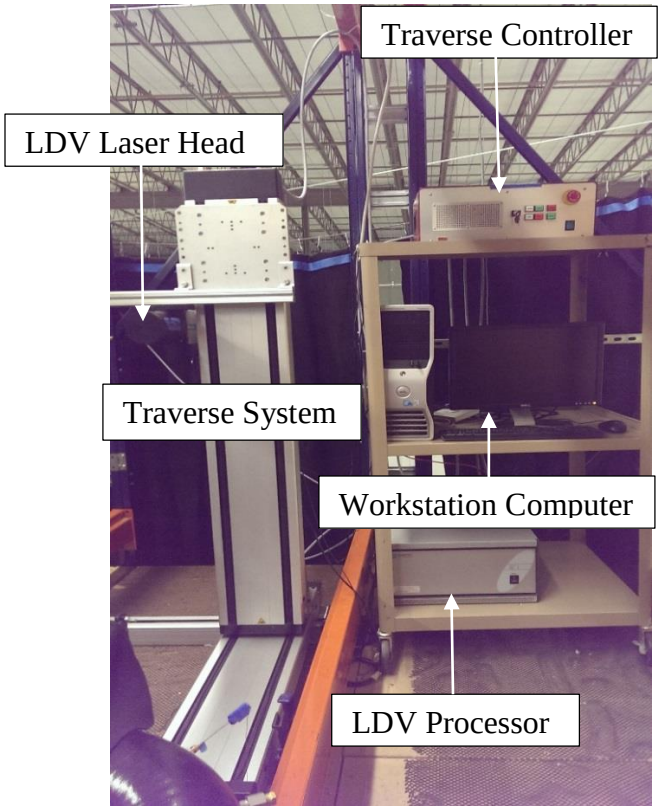

Figure 19. LDV experimental setup.

The laser head which is used is a Dantec Dynamics Standard FlowExplorer. It uses 35 mW lasers for measuring both the streamwise and spanwise velocity components. The head not only serves as a laser source, but also contains a photodetector in the backscattering configuration. Modularizing the system into one assembly has multiple benefits: 1) It saves considerable time from having to manually set up a detector, 2) only one transparent window is required to measure the flow, and 3) it allows for the movement of the laser head for measuring multiple points in space. Signals taken from the photodetector are received and transmitted to the processor. The processor is a Dantec Dynamics BSA F30 which allows for either burst acquisition or dead-time acquisition

modes. It is set to burst acquisition, in which any light received by the photodetector is converted into burst signals. Bursts which achieve a threshold signal-to-noise ratio are processed as data, while those which do not are filtered out. This mode is useful for making measurements with high-temporal resolution for either turbulent spectra or auto-correlation (BSA Flow Software v5.00). Processed signals are sent to the workstation computer, which are collected via the software. This software is the BSA Flow Software v5.03.00 by Dantec Dynamics. It is a robust program used for collecting, processing, storing, displaying, and post-processing acquired data for either LDV or Phase Doppler Anemometry (PDA) measurements. It is also used for varying some of the parameters for the laser head, processor, and traverse, and to input the coordinates for making measurements. Properties for the laser head and traverse system can be found in Table 5, and Figure 20 is a screenshot of the software user interface.

Table 5. LDV laser head and traverse system properties.

FlowExplorer Laser Head Properties		
LDA 1	Wavelength	660 nm
	Focal Length	500 mm
	Beam Diameter	2.2 mm
	Expander Ratio	1
	Beam Spacing	60 mm
	Frequency Shift	80 MHz
	Number of Fringes	34
	Fringe Spacing	5.51 µm
	Beam Half-Angle	3.434 °
	Probe Volume dX	0.1913 mm
	Probe Volume dY	0.191 mm
	Probe Volume dZ	3.189 mm
LDA 2	Wavelength	785 nm
	Focal Length	500 mm
	Beam Diameter	2.2 mm
	Expander Ratio	1
	Beam Spacing	60 mm
	Frequency Shift	80 MHz
	Number of Fringes	34
	Fringe Spacing	6.553 µm
	Beam Half-Angle	3.434 °
	Probe Volume dX	0.2276 mm
	Probe Volume dY	0.2272 mm
	Probe Volume dZ	3.793 mm
Traverse System Properties		
Range	X	110-2710 mm
	Y	110-2710 mm
	Z	110-2710 mm
Maximum Speed	X	25 mm/s
	Y	25 mm/s
	Z	25 mm/s
Maximum Load	X	175 Nm
	Y	150 Nm
	Z	340 Nm
Lift Capacity		60 kg

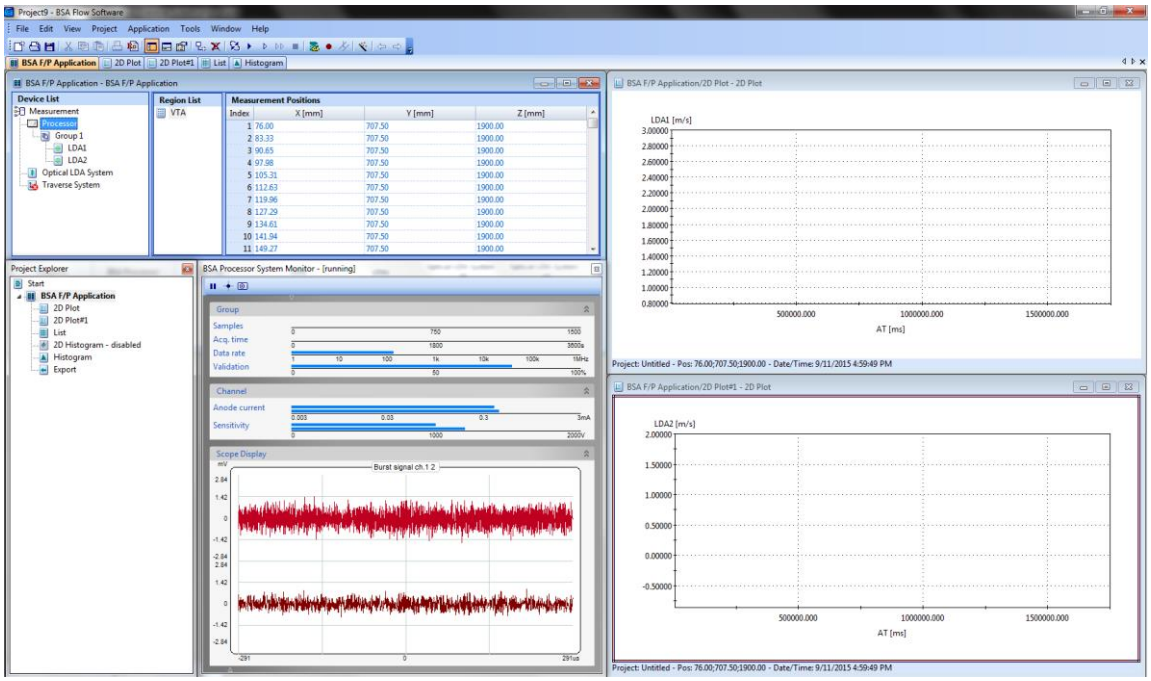

Figure 20. BSA Flow software user interface.

Before conducting preliminary experiments, it was necessary to fix, align, and calibrate the position of the traverse in order to: 1) grant the laser head access to all required data points, 2) convert the physical position of the laser head measurement volume into the proper coordinates for the BSA Flow software and back again into the post-processing software, and 3) ensure the safe operation of the traverse system by removing any potential obstructions. The initial fixing and aligning of the traverse was done iteratively using a "square" measuring rod to compare the distance of the front x-axis traverse rail relative to the upper plenum front face. This was done to within 1/8" (3.175 mm) of either end of the upper plenum relative to the traverse, which assures an angular tolerance of $\delta\theta = \pm 0.5^{o}$. Once properly aligned, the traverse was fixed by

bolting many 90^o brackets into the floor. These were used to sandwich the x-axis and y-axis traverse rail, making them immobile. The alignment was checked again after fixing was complete and no measureable difference was found.

The calibration of the position of the measurement volume was also done iteratively. This process involved carefully placing flat metal plates inside the upper plenum, in close alignment with the vertical and horizontal planes used for PIV and temperature measurements. Through much trial and error, an acceptable tolerance for the positions in the x, y, and z directions was found, which is a maximum of $\delta x = \delta y = \delta z = \pm 2$ mm. In addition, these measurements allowed for the establishment of a coordinate system, which was used for the coordinate transformation between the traverse system's coordinates and the post-processing software's coordinates.

The software used to post-process the raw LDV data was a script written in Matlab. Its first function was to transform the traverse coordinates for each data point into the physical coordinates of the upper plenum. Then, it needed to calculate the required parameters for each data point such as average velocity, turbulent intensity, normalized Reynolds stress, standard deviation, and standard error. The equations used for calculating each of these quantities are listed blow, which apply to both the spanwise and streamwise components of velocity (except for the Reynolds stress).

For the normalized average velocity, the equation goes as follows:

$$\frac{\langle U \rangle}{\langle U \rangle_{max}} = \frac{\sum_{i=1}^{N} u_i}{N \langle U \rangle_{max}}$$

Where ⟨U⟩ is the averaged velocity, u_i is the instantaneous velocity, N is the number of samples per data point, and $\langle U \rangle_{max}$ is the maximum velocity among all of the averaged data points. For the turbulent intensity, the following was used for calculations:

$$TI_U = \frac{\langle U' \rangle}{\langle U \rangle_{max}} = \frac{\sqrt{\frac{1}{N}\sum_{i=1}^{N}[u_i']^2}}{\langle U \rangle_{max}}$$

Where TI_U is the turbulent intensity, $\langle U' \rangle$ is the RMS value of the fluctuation, and u_i' is the instantaneous fluctuation. The normalized Reynolds stress was calculated as follows:

$$\frac{\langle U' \cdot V' \rangle}{\langle U \rangle_{max}^2} = \frac{\frac{1}{N}\sum_{i=1}^{N}\{[u_i'][v_i']\}}{\langle U \rangle_{max}^2}$$

Where $\langle U' \cdot V' \rangle$ is the Reynolds stress, u_i' is the streamwise instantaneous fluctuation, and v_i' is the spanwise instantaneous fluctuation. Next, the standard deviation for each data point was calculated as follows:

$$\sigma = \sqrt{\frac{\sum_{i=1}^{N}(u_i - \langle \mathrm{U} \rangle)}{N-1}}$$

Where σ is the standard deviation. Finally, the normalized standard error is calculated as follows:

$$\frac{\delta u}{\langle U \rangle_{max}} = \frac{\sigma}{\langle U \rangle_{max}\sqrt{N}}$$

Where δu is the standard error.

Once the coordinates for all measurement planes was recorded into the software, the experimental test matrix was decided upon. Of the cases involved in the original test

matrix (Table 6), it was decided that Case 1a and Case 1 would serve as the base cases for future LDV experiments. These cases were chosen for several reasons, including: 1) They both involved all four risers in operation, 2) they allowed comparisons between an adiabatic and heated case, 3) they did not involve reverse flow phenomena, and 4) the quality of PIV data was initially found to be of good quality, which could allow for good comparisons between it and the LDV data. Particularly for 3), it was desired not to include cases involving reverse flow phenomena, which would make comparisons between heated and adiabatic cases more complex. However, future LDV experiments will undoubtedly investigate the reverse flow cases.

Table 6. Experimental test matrix used for previous PIV and temperature measurements. LDV experiments are shown with bolded text.

Original Experimental Test Matrix			
Case	Riser	Inlet Velocity (m/s)	Inlet Temperature (°C)
1a	**All**	**5**	**Ambient**
2a	Riser ④	5	Ambient
3a	All	2.25	Ambient
4a	Riser ④	2.25	Ambient
1	**All**	**5**	**120**
2	Riser ④	5	120
3	All	2.25	120
4	Riser ④	2.25	120

With the cases selected, it was then decided at which experimental planes the measurements would take place. Ideally, data would be taken at all planes, though

involving more planes would require reduction in the number of data points taken at each. Also, since both cases did not involve reverse flow, only plane VTA would be significant for the analysis. Thus, the test matrix was decided to be Case 1a and Case 1 with data taken at plane VTA. Next came the decision of where in VTA data should be taken. It was desired to take line profiles at several elevations which would show the behavior of the jets as they merged. These profiles were decided to be located at the same elevations as those of the horizontal planes HTA-HTC, as well as at the center of the chimney exhausts. Given this, there are a total of four elevations used for the experiments. The number of data points at each elevation was still to be determined. Before this could be done, the optimal settings for the acquisition software were found. This was required since these settings would influence the data acquisition rate, which would be a primary factor in determining how many data points were to be used per experiment. Also, it was desired to minimize noise in the acquisition, which was done by maximizing the signal to noise ratio (SNR). These settings were found though preliminary experiments. Afterwards, the final settings used for data acquisition were decided on, which are featured in Table 7.

Table 7. LDV software settings used for experiments.

LDV Acquisition Software Settings		
General Options	Disable Traverse?	No
	Prompt before region?	No
	Prompt before position?	Yes
	Bypass errors	No
	Delay between positions	60 s
	Delay between positions	0 s
Processor	Acquisition Mode	Burst
Group 1	Max Samples	1500
	Max Acquisition Time	3600 s
LDA 1	Center Velocity	0 m/s
	Velocity Span	10.33105 m/s
	Sensitivity	1000 V
LDA 2	Center Velocity	0 m/s
	Velocity Span	4.60788 m/s
	Sensitivity	1200 V
Traverse System-Ch 1-3	Speed	25 mm/s
	Calibration Factor	160
	Home Speed	25 mm/s

With the optimal software settings in use, the average data rate was found to be 5 Hz. From this, an estimate was made to find the maximum number of data points to be used for each experiment. Preliminary experiments were required to find the number of samples needed for each data point to be of good statistical quality. Figure 21 shows the results of one such experiment, which involved taking 10e5 samples at a single location

and calculating the standard error percentage as a function of sample number. It is seen that after 1000 samples the error drops to approximately one percent. To achieve less than one percent standard error, it was decided that 1500 samples would be sufficient. With an acquisition rate of 5 Hz and having each experiment to run an estimated time of 16 hours, the total number of data points was 192 data points. Running experiments for more time would yield more data points, though the experiments were required to run for the minimal amount of time needed. Thus, 200 data points were decided on, with 50 points for each elevation. These points were spaced apart evenly between the ends of the riser 1 and riser 4 inlet ducts, ranging from x = 0.134 m to x = 0.314 m. This was made so the measurements would capture the vast majority of the jet profiles.

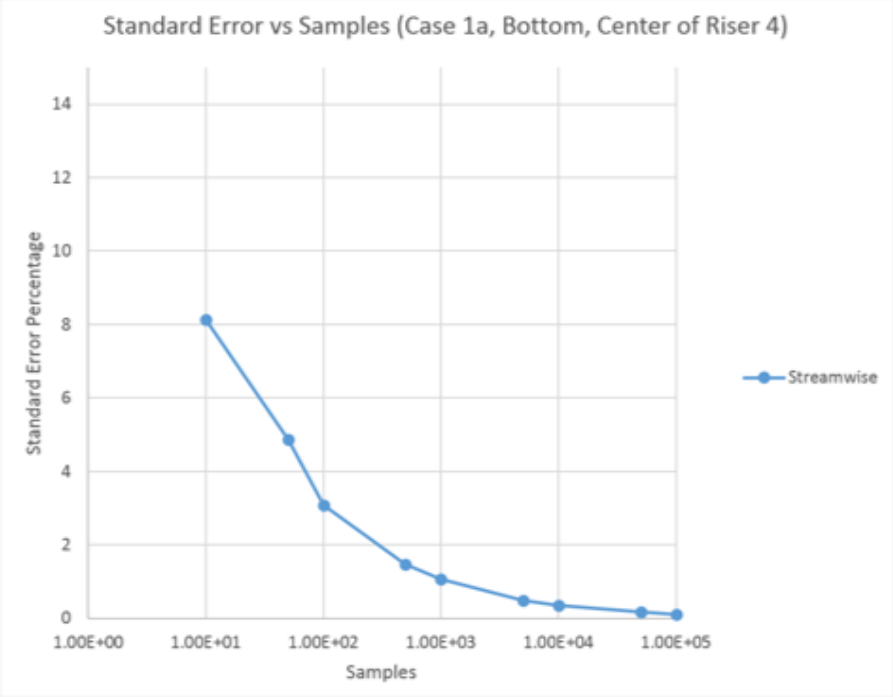

Figure 21. Preliminary experiment performed to estimate standard error for measurements based on number of samples.

Once the all parameters for the experiments were well defined, it was time to acquire data though running experiments. The procedure for obtaining steady-state conditions, both adiabatic and heated, has been previously outlined by Sulaiman (Sulaiman, 2015). Once the experimental conditions were met, the process of running the data acquisition system was relatively straightforward. This standard operating procedure is outlined as follows:

1) Once experimental conditions have been obtained, turn on the BSA processor and Traverse controller.
2) Turn on the desktop computer and laser head, but keep the cap on the laser head until laser is focused into upper plenum to prevent stray laser reflections.
3) Login onto computer and open the BSA Flow software.
4) Check the settings of the software to ensure correct acquisition.
5) Check the general area of the traverse system for any obstructions or obstacles prior to moving the traverse.
6) Move the traverse to the home switch to obtain a reference for the software's coordinate system.
7) Move the traverse to the starting position for the experiment.
8) Uncap the laser head and begin running the acquisition. Initially monitor for at least 10 minutes to assure correct operation of the software.
9) Periodically check-up on the facility to ensure experimental conditions and acquisition system are operating correctly.

10) Once acquisition is complete, turn off and cap the laser head and move the traverse back to the home switch.
11) Turn off the desktop computer, followed by turning off the BSA processor and traverse controller.
12) Turn off the necessary components of the facility.

5. RESULTS AND DISCUSSION

The results of the experiments for Case 1a and Case 1 are shown in the proceeding figures. Results from Case 1a are shown in Figures 22 through 44, and Figures 45 through 67 are the results from Case 1. For Case 1a, Figures 22 through 24 depict several graphs made in Tecplot, in which the streamwise velocity contour for PIV is plotted with overlaid velocity profiles. Figure 22 features line profiles of the LDV streamwise average vectors at the four elevations, Figure 23 features PIV streamwise average vectors which were extracted from the contour plot, and Figure 24 has both LDV and PIV vectors plotted simultaneously. This was done to give a qualitative look at the spatial location of the data, as well as perform preliminary comparisons between the LDV and PIV measurements; the more rigorous comparisons are done in the proceeding figures. It should be noted that Figures 45 through 47 for Case 1 correspond to Figures 22 through 24 for Case 1a. This correspondence between Case 1 and Case 1a is true for all plots. To minimize redundant explanations, all descriptions for future plots for Case 1a will also mention the corresponding Case 1 plots.

Figure 25 (Figure 48 for Case 1) is an excel plot of all four elevations for the LDV normalized streamwise average velocities, which are portrayed in terms of scalars and not vectors. Figure 26 (Figure 49 for Case 1) shows the corresponding PIV plot for the normalized streamwise average velocity. These were done to provide direct comparisons between the different elevations, which show the decaying and merging behavior of the jets as a function of elevation. It should be noted that all normalized PIV and LDV plots

are normalized with each measurement technique's respective maximum velocity and not the maximum velocity of both techniques.

Figures 27, 28, 29, and 30 (Figures 50, 51, 52, and 53 for Case 1) are Excel graphs of the comparisons between PIV and LDV for the normalized streamwise average velocity at the bottom, bottom-middle, top-middle, and top elevations, respectively. Figures 31, 32, 33, and 34 (Figures 54, 55, 56, and 57 for Case 1) are Excel graphs of the comparisons between PIV and LDV for the spanwise turbulent intensities at the bottom, bottom-middle, top-middle, and top elevations, respectively. Figures 35, 36, 37, and 38 (Figures 58, 59, 60, and 61) are Excel graphs of the comparisons between PIV and LDV for the streamwise turbulent intensities at the bottom, bottom-middle, top-middle, and top elevations, respectively. Figures 39, 40, 41, and 42 (Figures 62, 63, 64, and 65 for Case 1) are Excel graphs of the comparisons between PIV and LDV of the normalized Reynolds stresses at the bottom, bottom-middle, top-middle, and top elevations, respectively.

Lastly are the results from the repeatability experiments, which are featured in Figures 43 and 44 (Figures 66 and 67 for Case 1). For these experiments, two elevations, bottom and bottom-middle, were chosen for analyzing the stability of the system under steady-state conditions over an extended period of time. At each elevation 12 data points were selected, 8 which lie directly above the edge of each riser inlet and 4 directly above the center of each riser inlet. Each data point was taken as a regular data point, with 1500 samples per data point at 5 Hz data rate. After taking data at both elevations, the experiment was repeated 4 additional times. This allowed for acquiring 5 independent data sets, between which the average velocity and standard deviation percentage (percentage

of the average velocity of that data point) were calculated and plotted. These experiments lasted approximately 24 hours, which was seen as a good basis for measuring the system stability. Figure 43 (Figure 66 for Case 1) is a plot of the average streamwise velocities, and Figure 44 (Figure 67 for Case 1) is a plot of the standard deviation percentages.

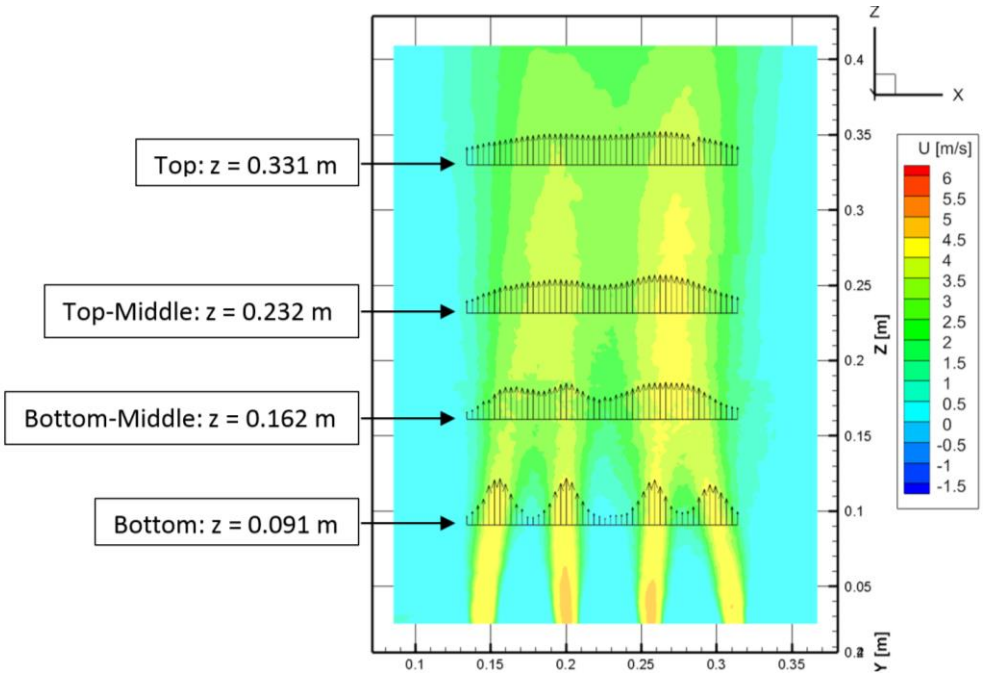

Figure 22. Case 1a, VTA - PIV Contour with LDV average streamwise vectors overlaid (black vectors).

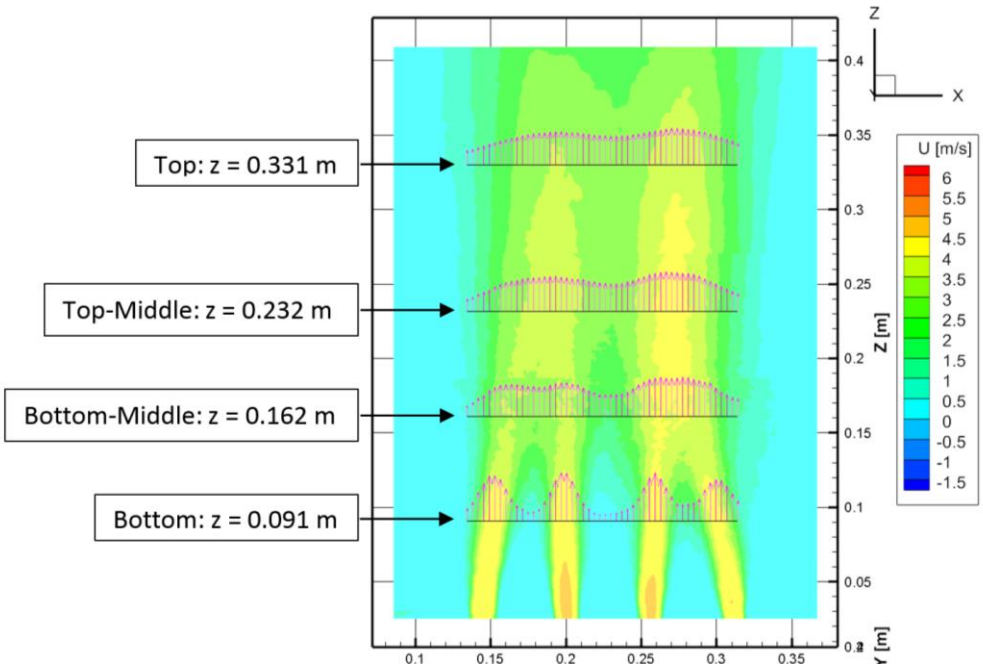

Figure 23. Case 1a, VTA - PIV Contour with PIV average streamwise vectors overlaid (red vectors).

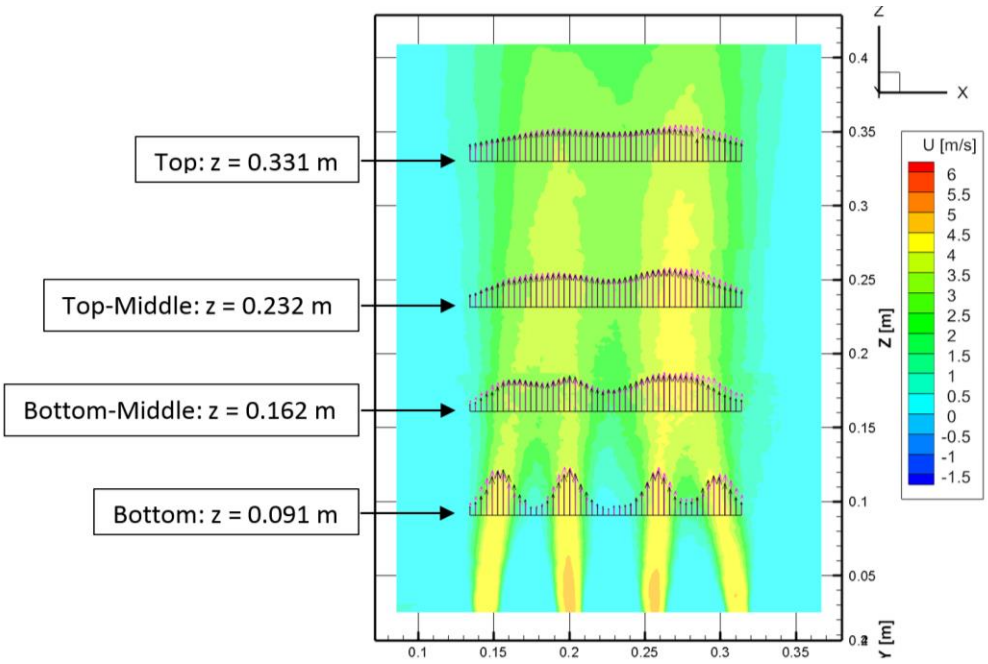

Figure 24. Case 1a, VTA - PIV Contour with LDV and PIV average streamwise vectors simultaneously overlaid.

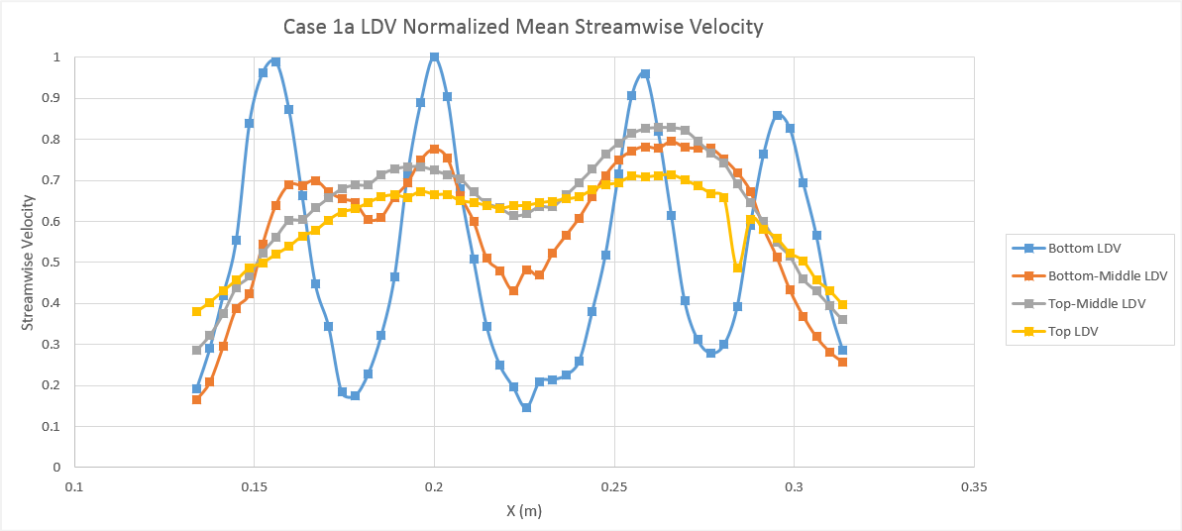

Figure 25. Case 1a – LDV normalized average streamwise velocities plotted for all four elevations.

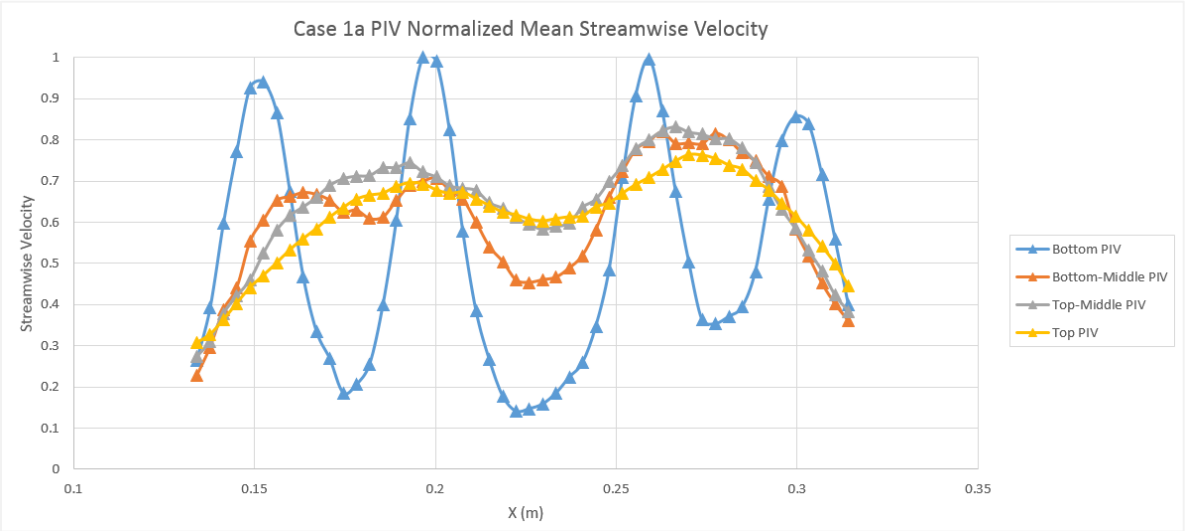

Figure 26. Case 1a – PIV normalized average streamwise velocities plotted for all four elevations.

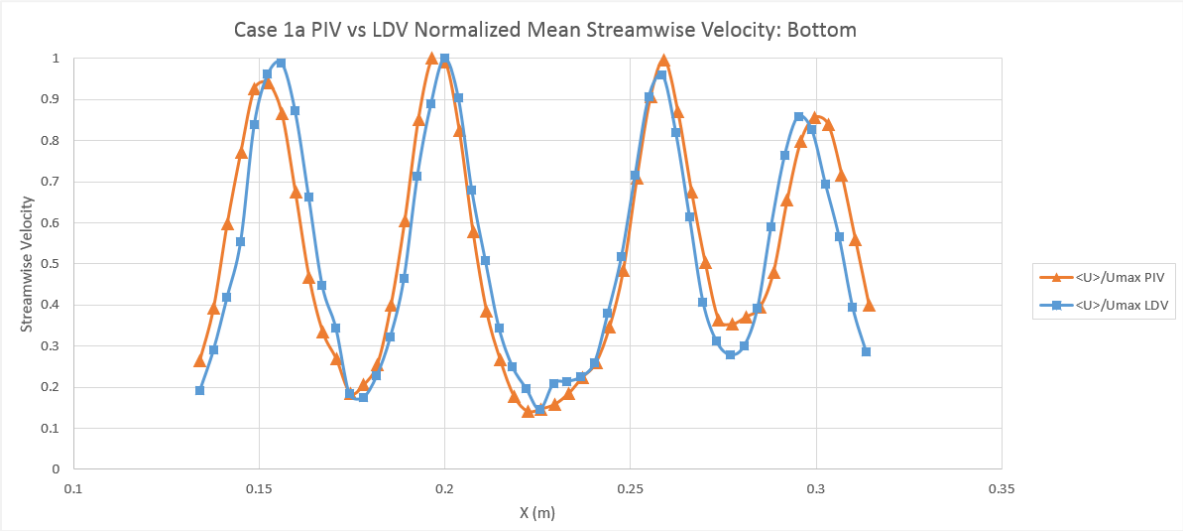

Figure 27. Case 1a – PIV vs LDV normalized average streamwise velocities plotted at bottom elevation (z = 0.091 m).

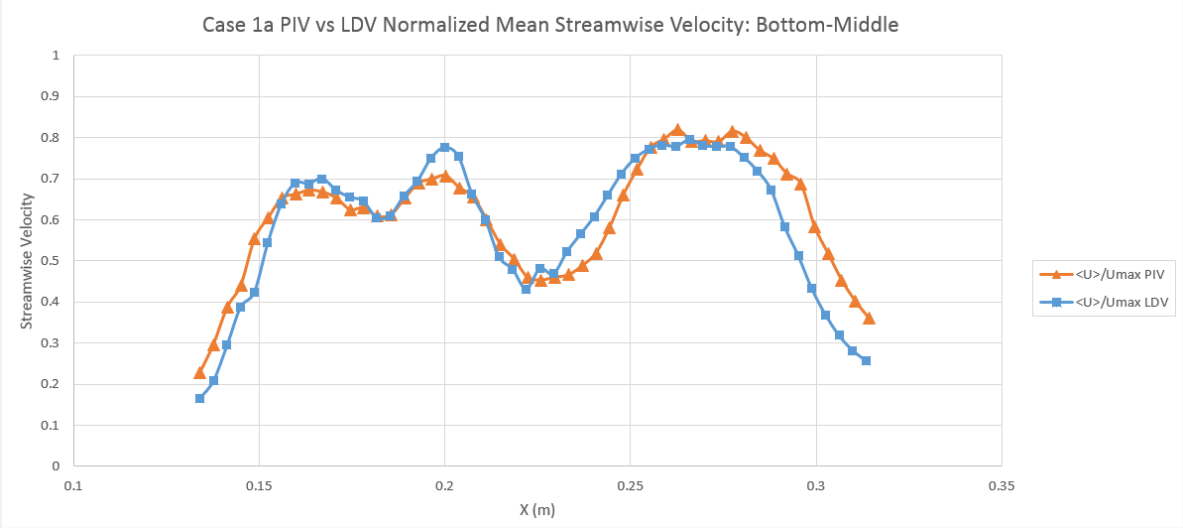

Figure 28. Case 1a – PIV vs LDV normalized average streamwise velocities plotted at bottom-middle elevation (z = 0.162 m).

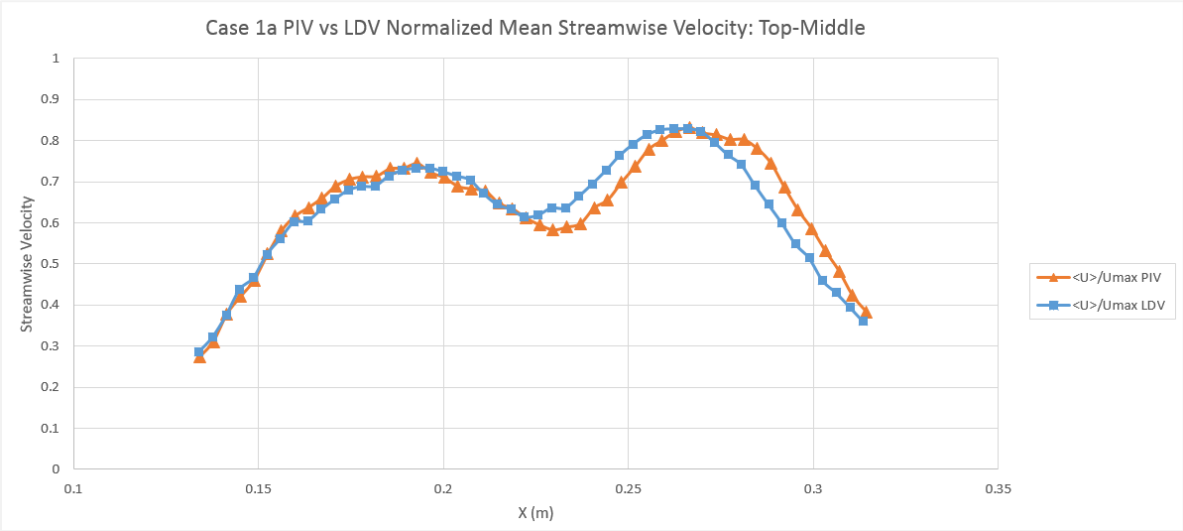

Figure 29. Case 1a – PIV vs LDV normalized average streamwise velocities plotted at top-middle elevation (z = 0.232 m).

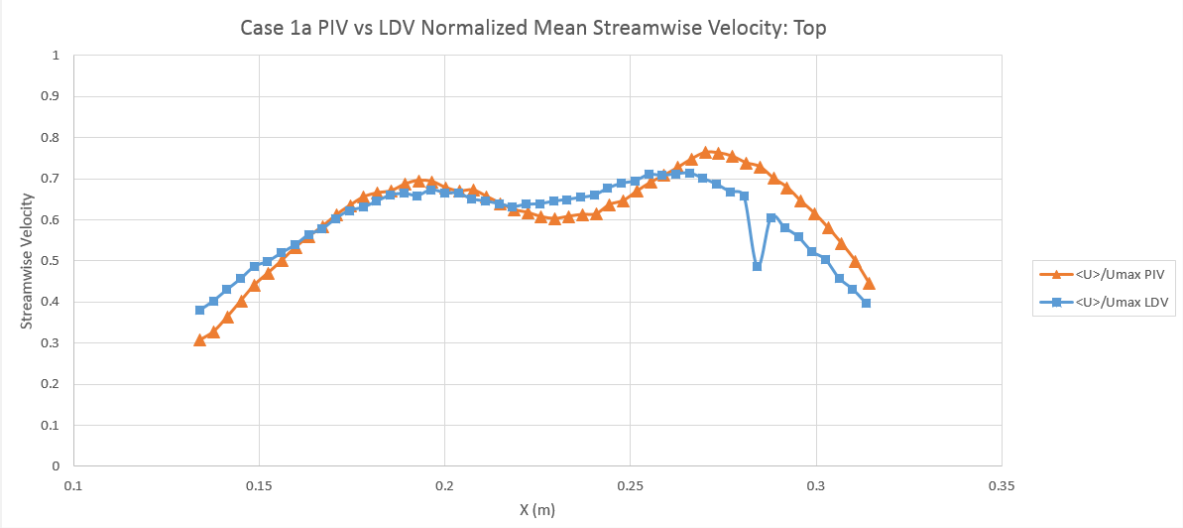

Figure 30. Case 1a – PIV vs LDV normalized average streamwise velocities plotted at top elevation (z = 0.331 m).

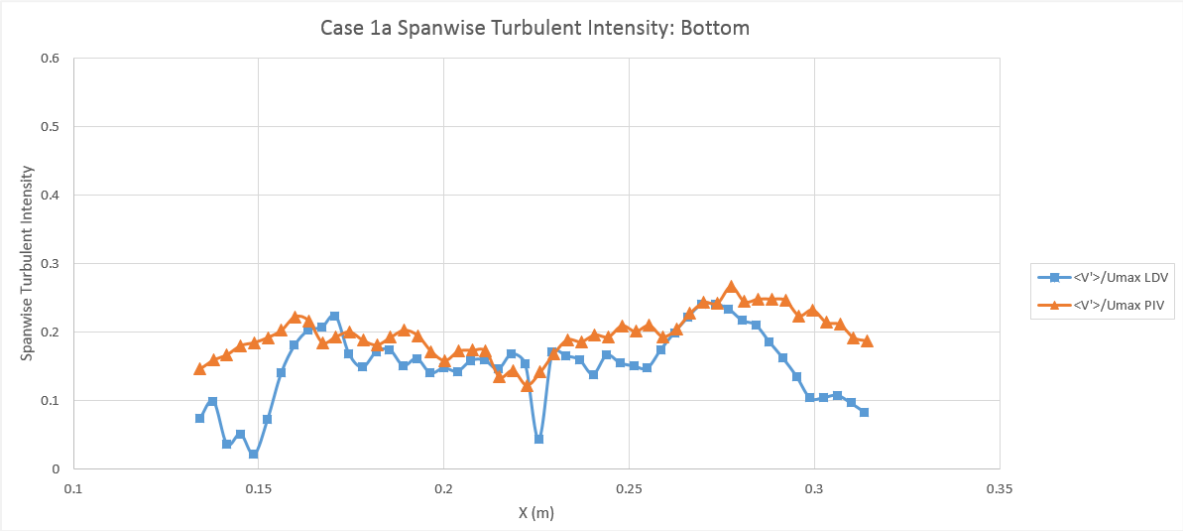

Figure 31. Case 1a – PIV vs LDV average spanwise turbulent intensity plotted at bottom elevation (z = 0.091 m).

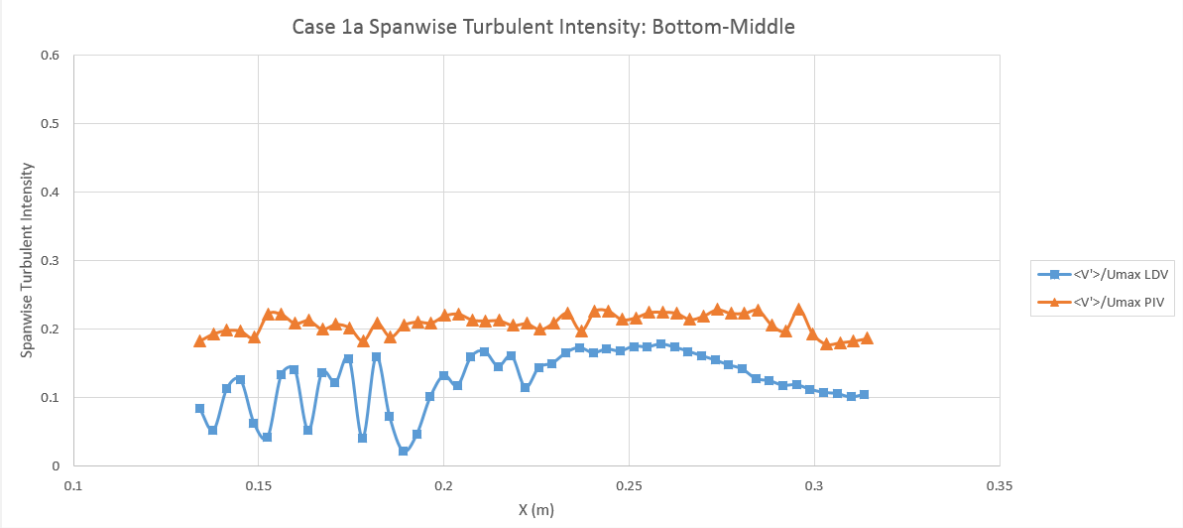

Figure 32. Case 1a – PIV vs LDV average spanwise turbulent intensity plotted at bottom-middle elevation (z = 0.162 m).

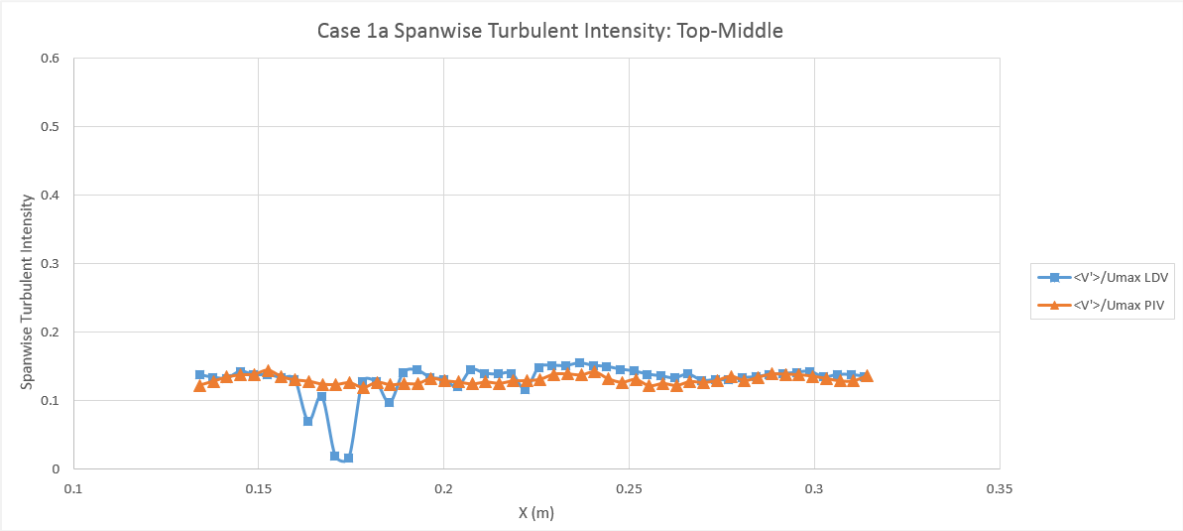

Figure 33. Case 1a – PIV vs LDV average spanwise turbulent intensity plotted at top-middle elevation (z = 0.232 m).

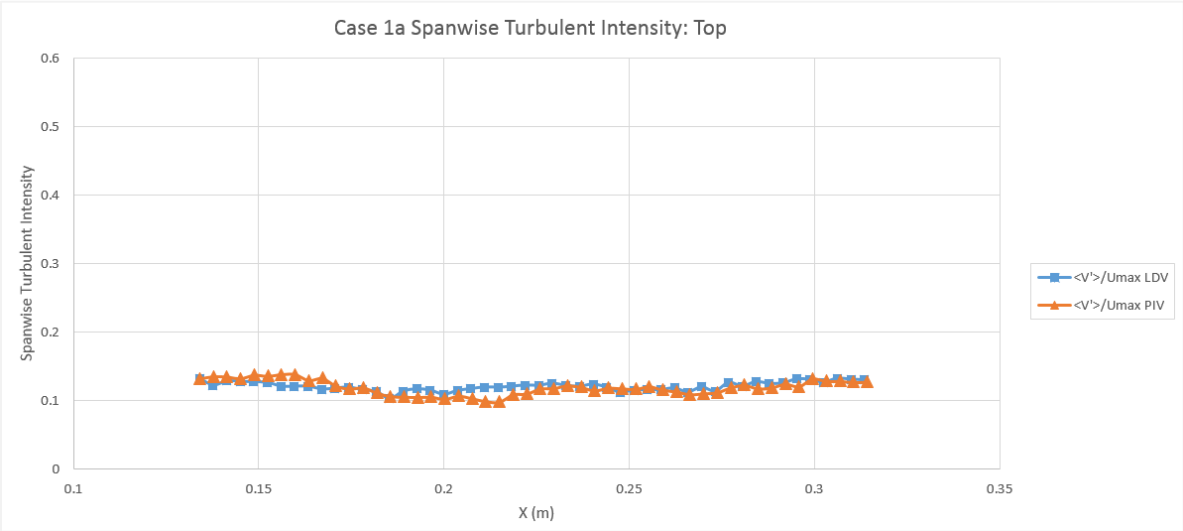

Figure 34. Case 1a – PIV vs LDV average spanwise turbulent intensity plotted at top elevation (z = 0.331 m).

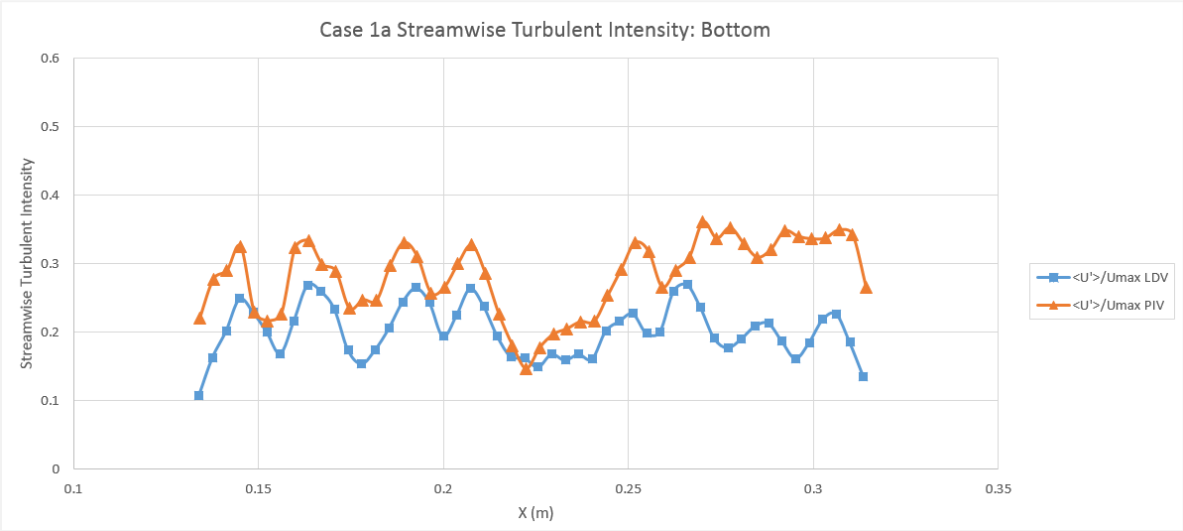

Figure 35. Case 1a – PIV vs LDV average streamwise turbulent intensity plotted at bottom elevation (z = 0.091 m).

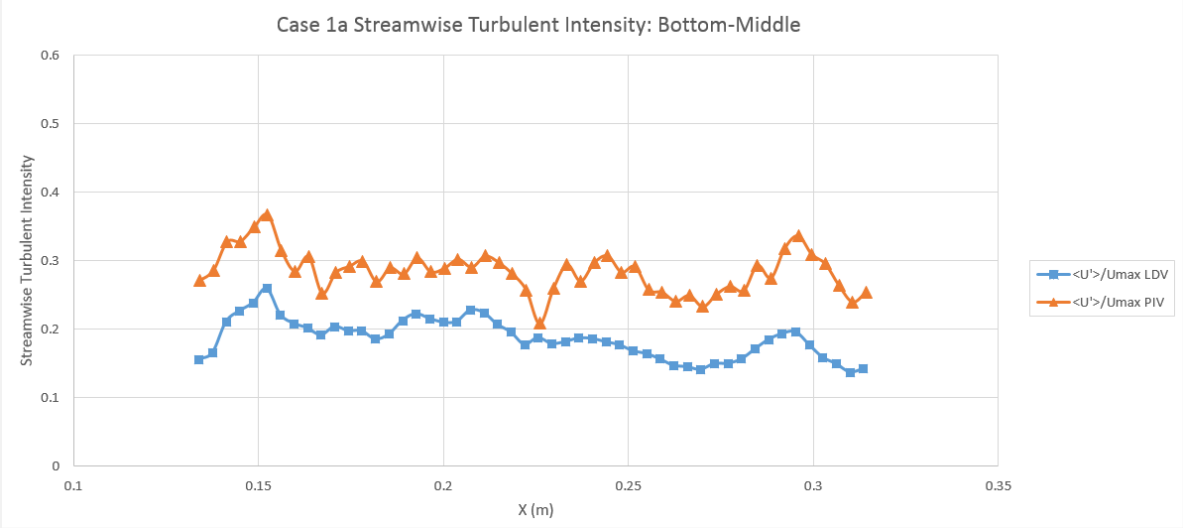

Figure 36. Case 1a – PIV vs LDV average streamwise turbulent intensity plotted at bottom-middle elevation (z = 0.162 m).

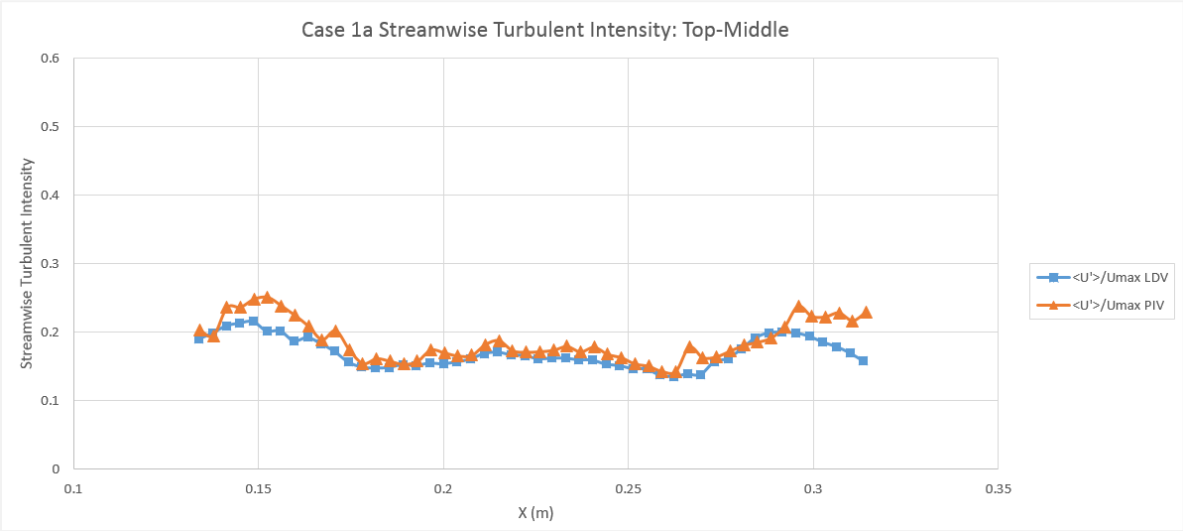

Figure 37. Case 1a – PIV vs LDV average streamwise turbulent intensity plotted at top-middle elevation (z = 0.232 m).

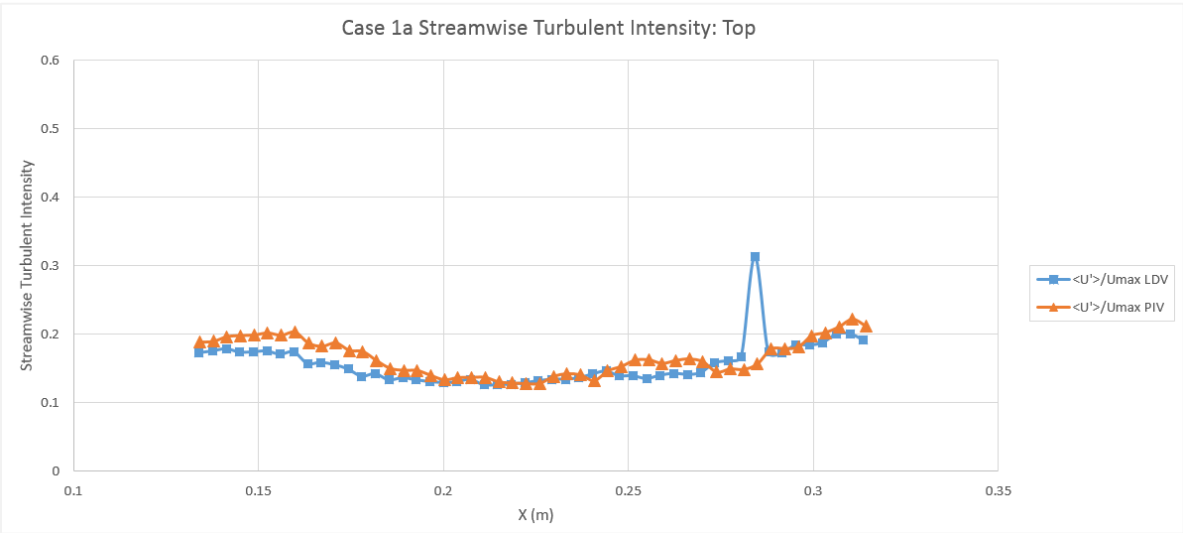

Figure 38. Case 1a – PIV vs LDV average streamwise turbulent intensity plotted at top elevation (z = 0.331 m).

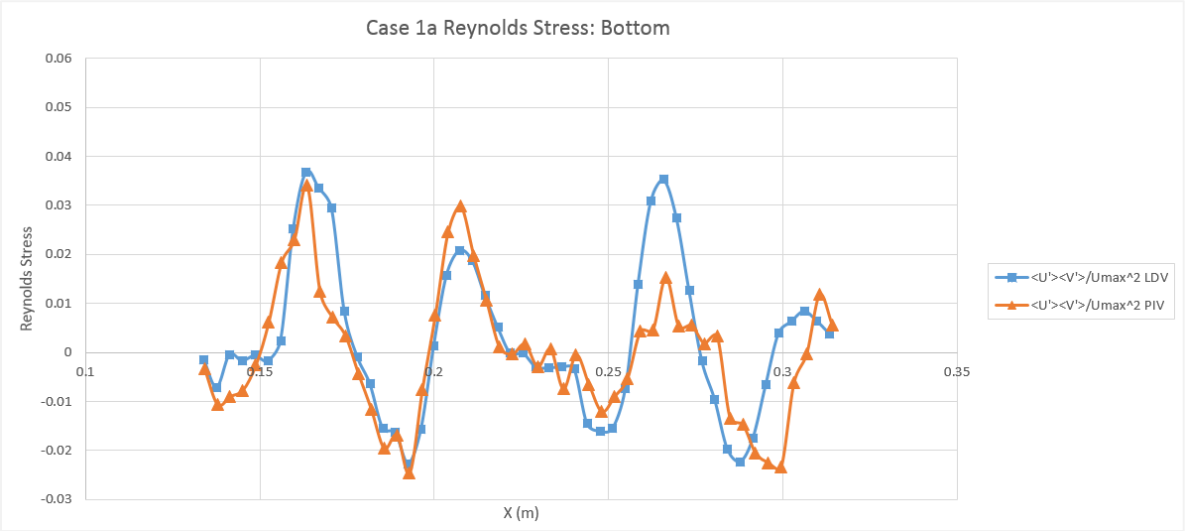

Figure 39. Case 1a – PIV vs LDV average Reynolds stress plotted at bottom elevation (z = 0.091 m).

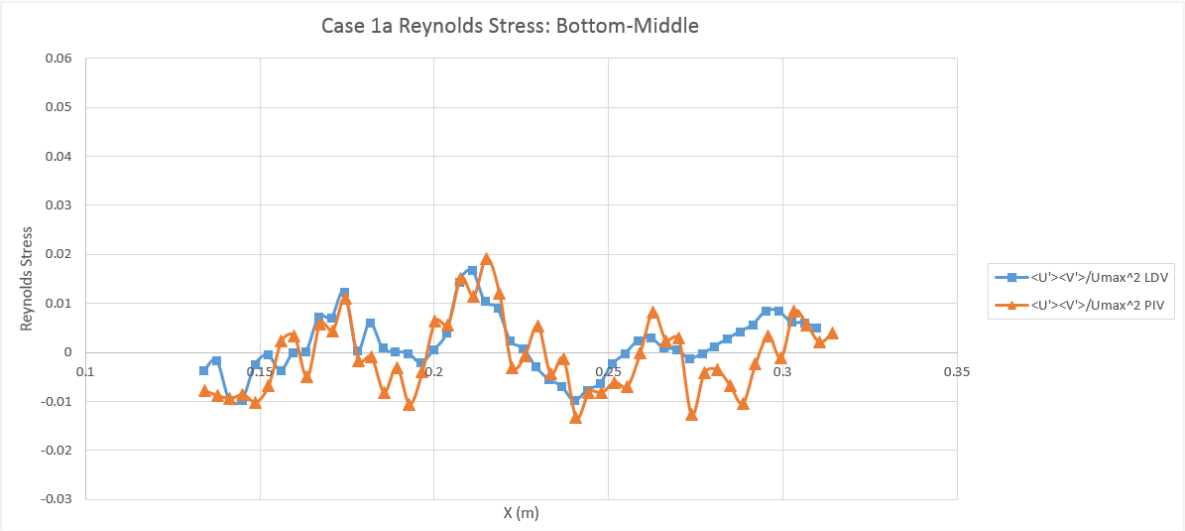

Figure 40. Case 1a – PIV vs LDV average Reynolds stress plotted at bottom-middle elevation (z = 0.162 m).

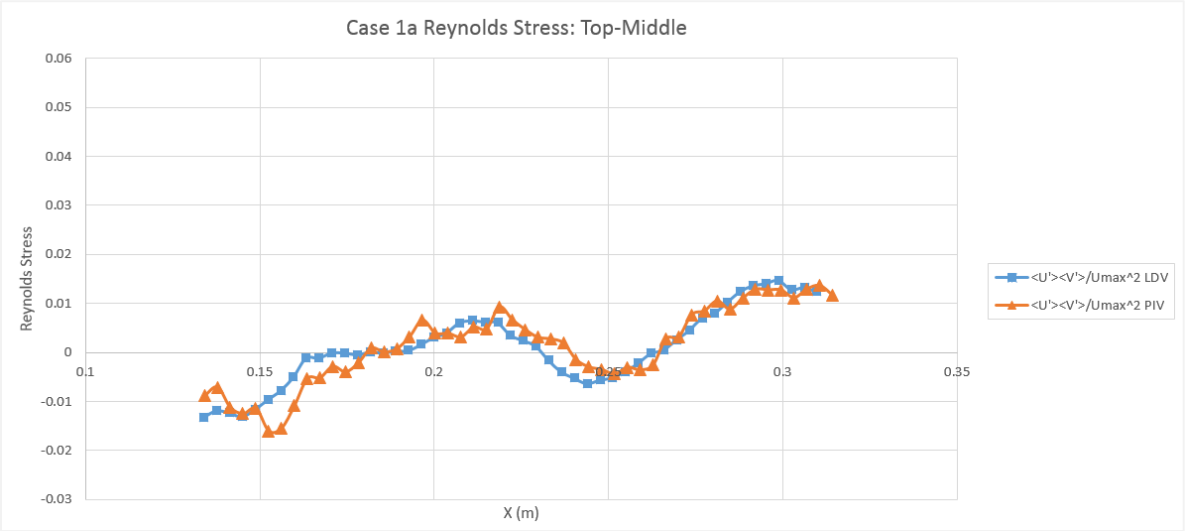

Figure 41. Case 1a – PIV vs LDV average Reynolds stress plotted at top-middle elevation (z = 0.232 m).

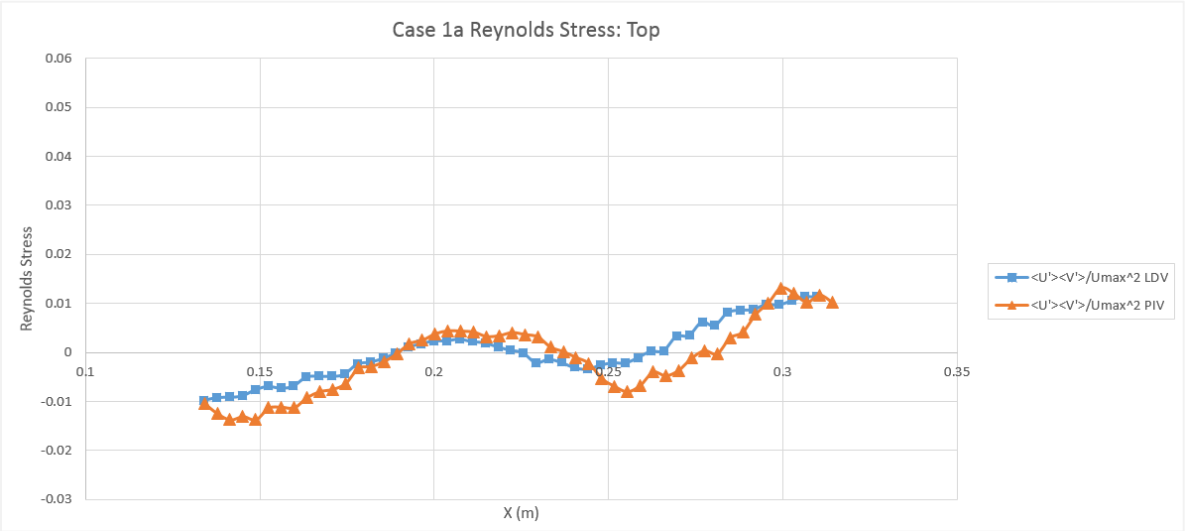

Figure 42. Case 1a – PIV vs LDV average Reynolds stress plotted at top elevation (z = 0.331 m).

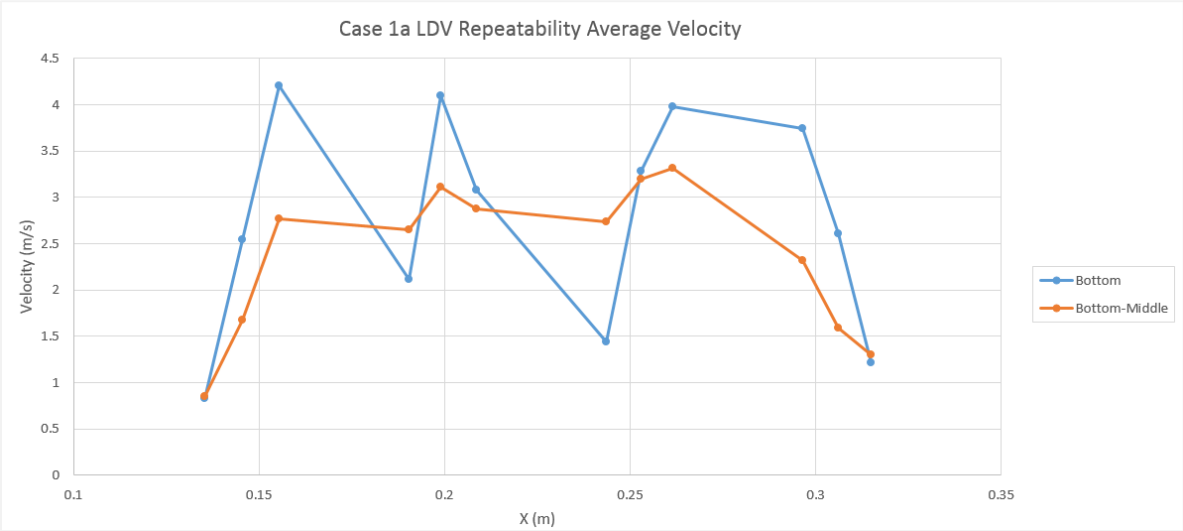

Figure 43. Case 1a – LDV repeatability average velocity for bottom and bottom-middle elevations (z = 0.091 m and z = 0.162 m, respectively).

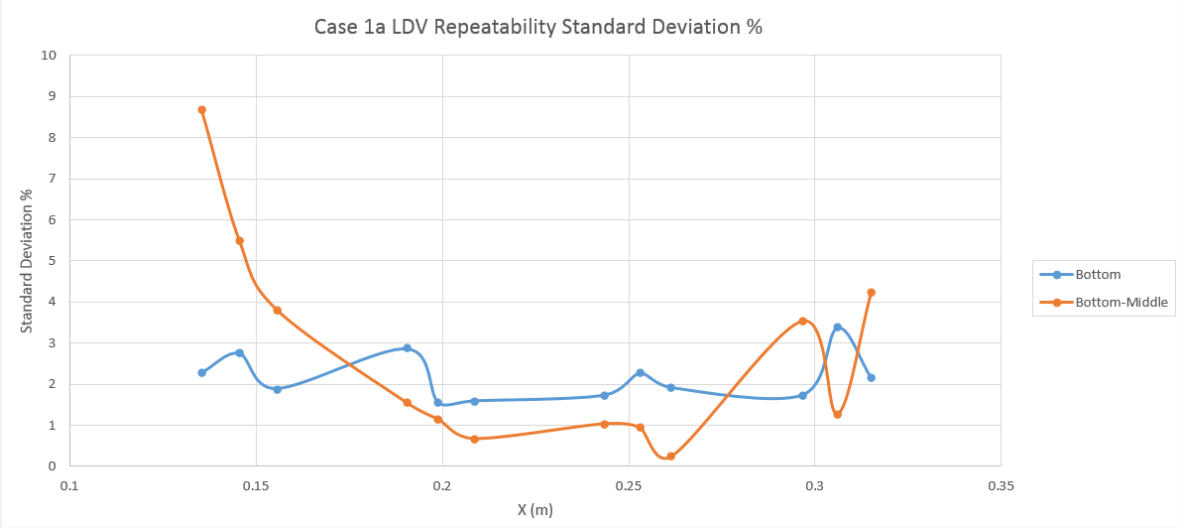

Figure 44. Case 1a – LDV repeatability standard deviation percentage for bottom and bottom-middle elevations (z = 0.091 m and z = 0.162 m, respectively).

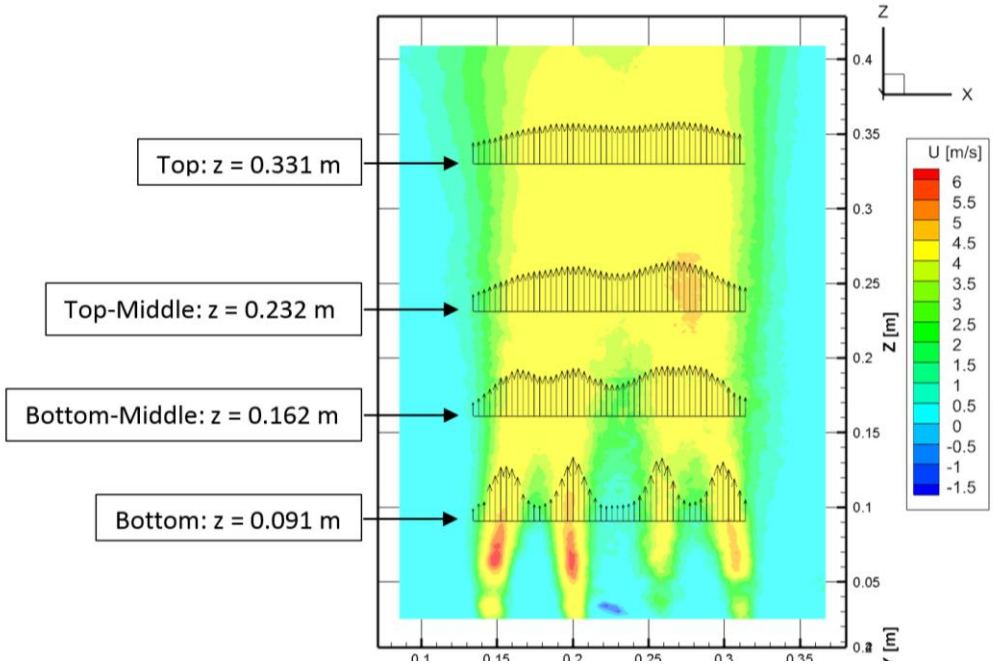

Figure 45. Case 1, VTA - PIV Contour with LDV average streamwise vectors overlaid (black vectors).

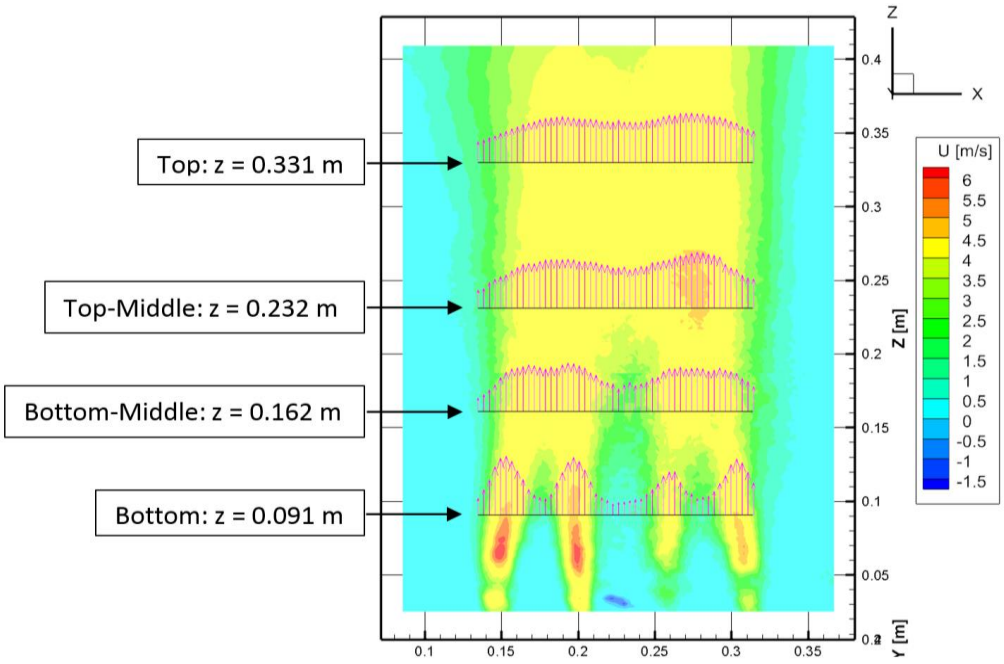

Figure 46. Case 1, VTA - PIV Contour with PIV average streamwise vectors overlaid (red vectors).

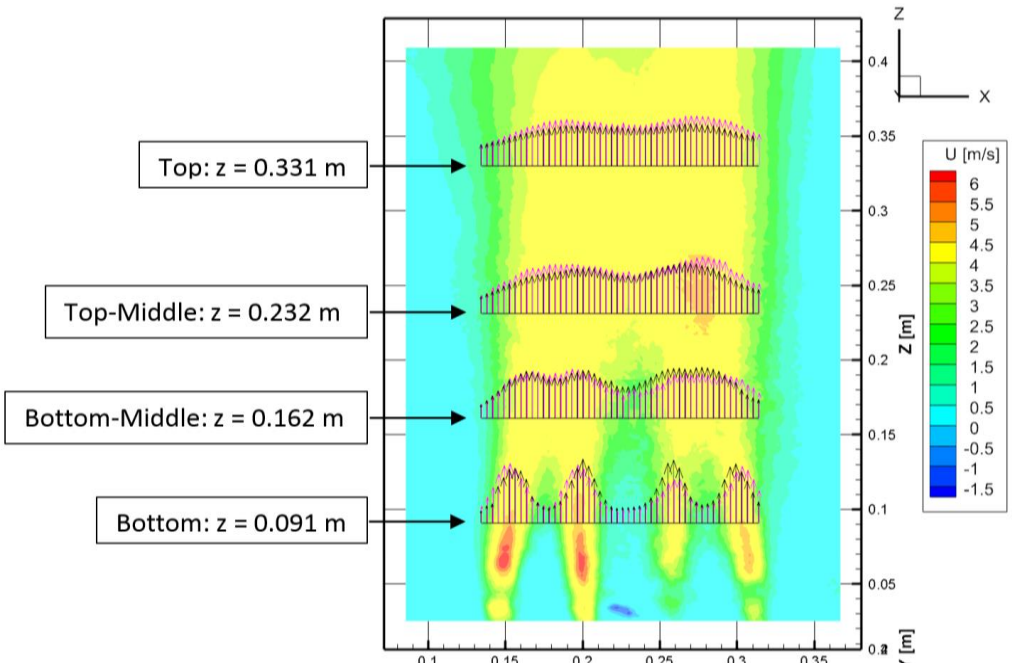

Figure 47. Case 1, VTA - PIV Contour with LDV and PIV average streamwise vectors simultaneously overlaid.

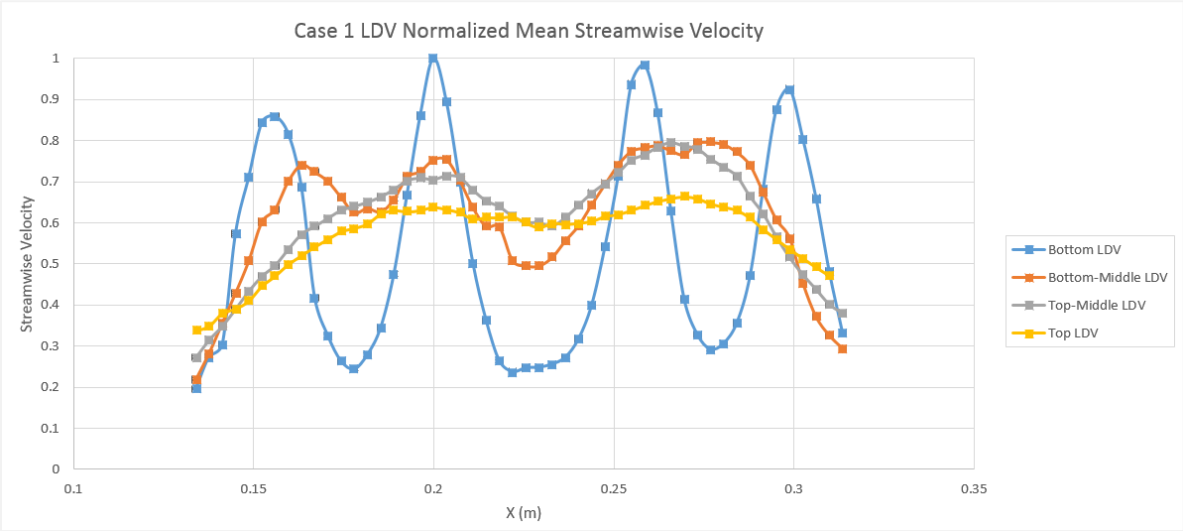

Figure 48. Case 1 – LDV normalized average streamwise velocities plotted for all four elevations.

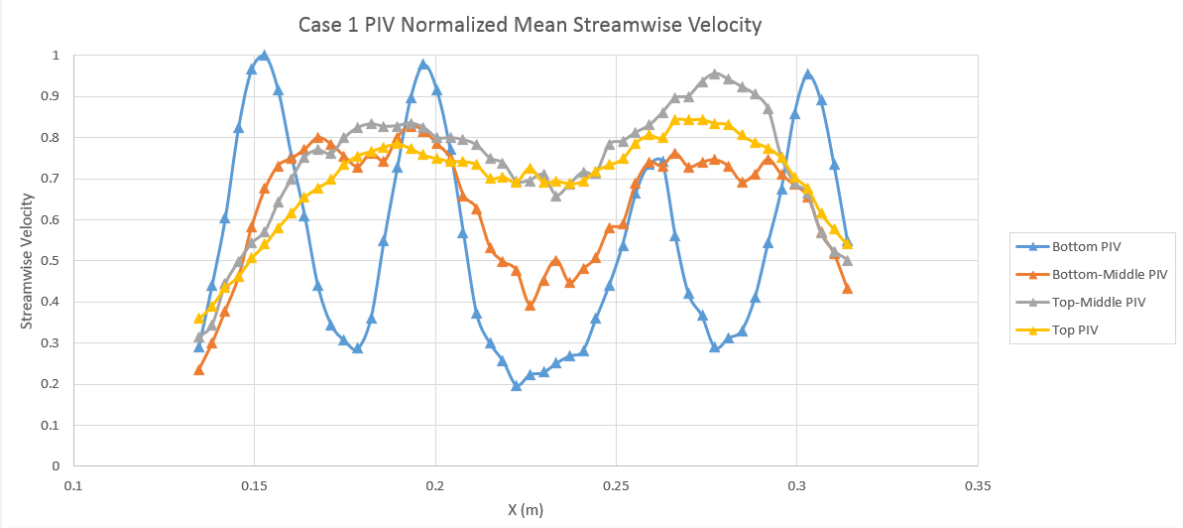

Figure 49. Case 1 – PIV normalized average streamwise velocities plotted for all four elevations.

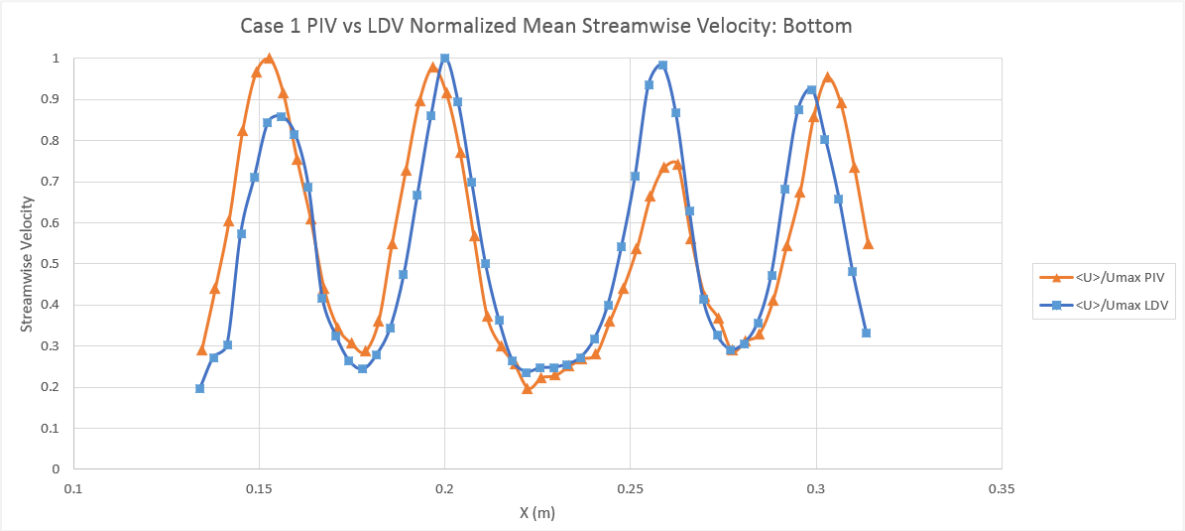

Figure 50. Case 1 – PIV vs LDV normalized average streamwise velocities plotted at bottom elevation (z = 0.091 m).

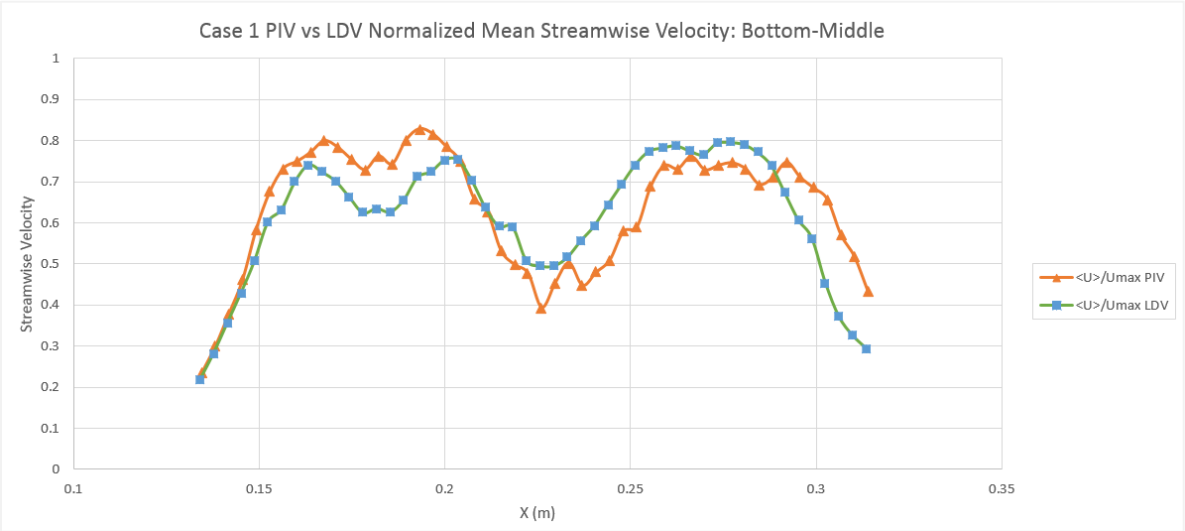

Figure 51. Case 1 – PIV vs LDV normalized average streamwise velocities plotted at bottom-middle elevation (z = 0.162 m).

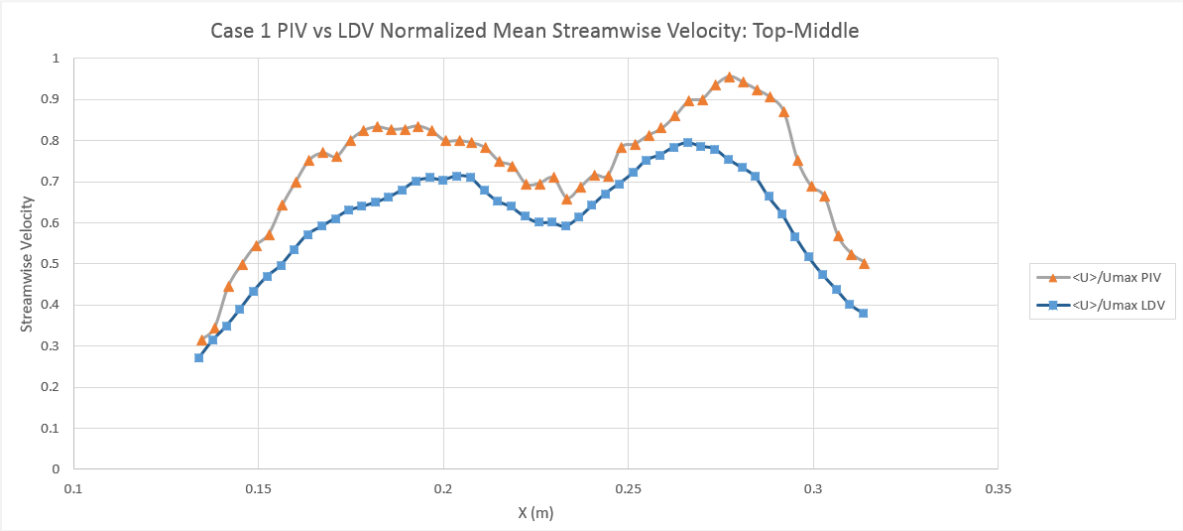

Figure 52. Case 1 – PIV vs LDV normalized average streamwise velocities plotted at top-middle elevation (z = 0.232 m).

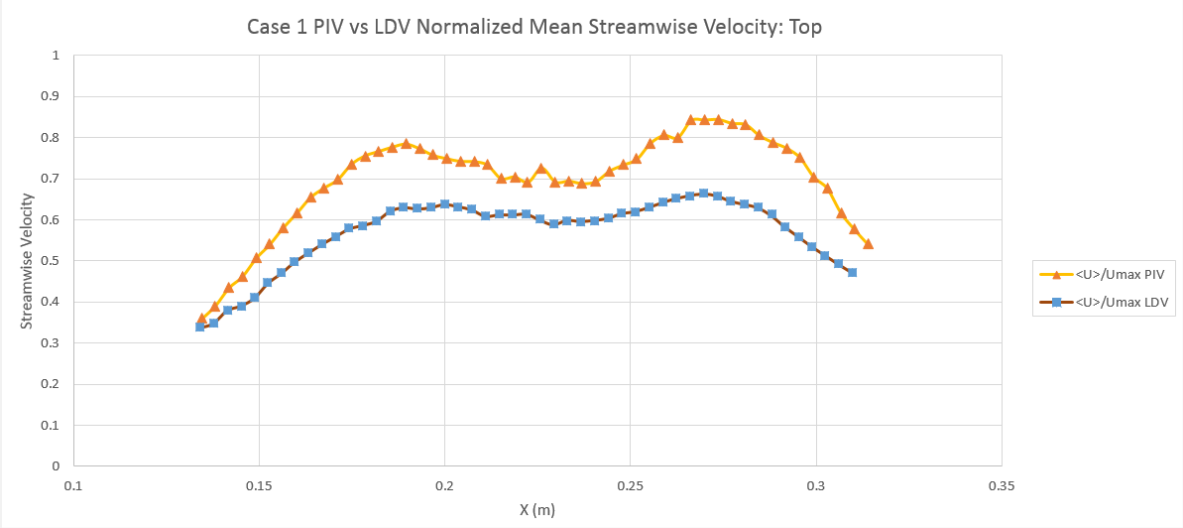

Figure 53. Case 1 – PIV vs LDV normalized average streamwise velocities plotted at top elevation (z = 0.331 m).

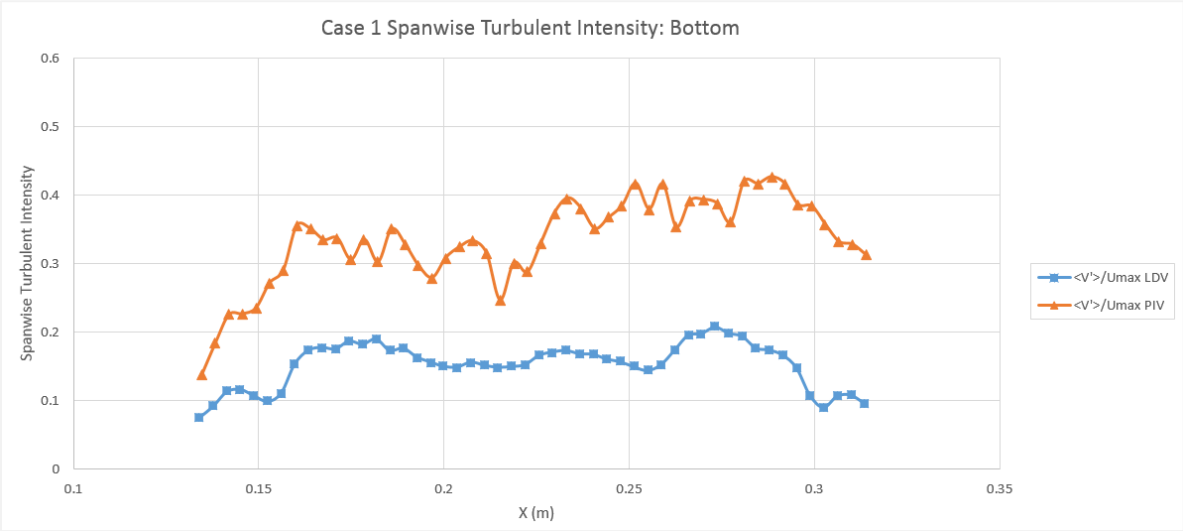

Figure 54. Case 1 – PIV vs LDV average spanwise turbulent intensity plotted at bottom elevation (z = 0.091 m).

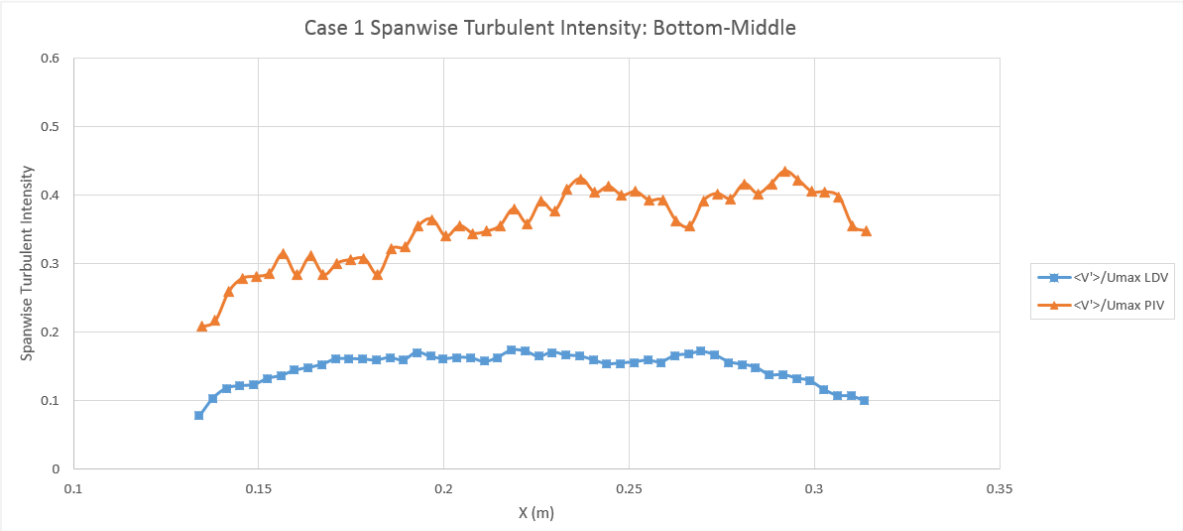

Figure 55. Case 1 – PIV vs LDV average spanwise turbulent intensity plotted at bottom-middle elevation (z = 0.162 m).

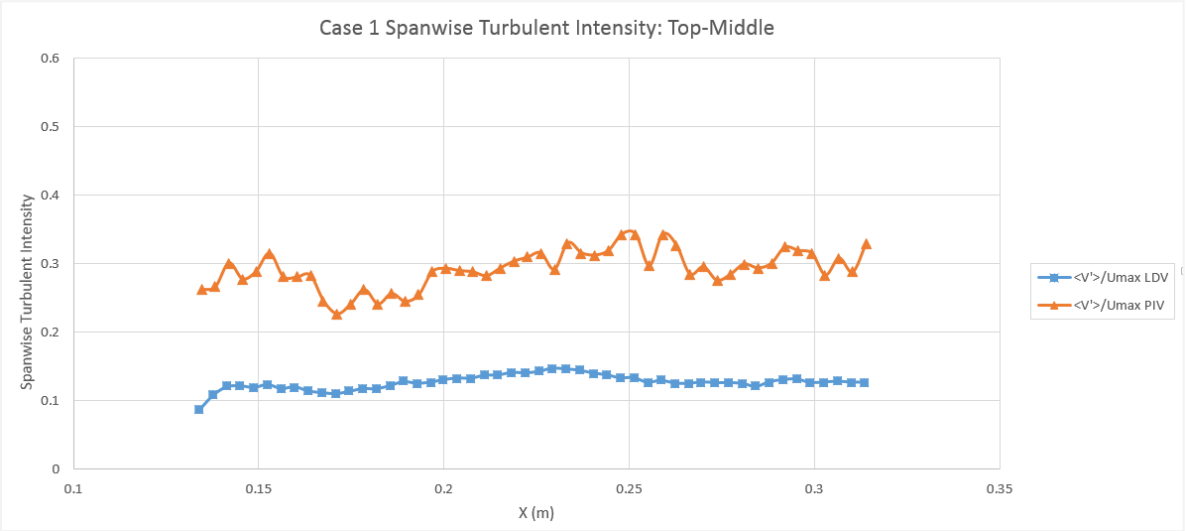

Figure 56. Case 1 – PIV vs LDV average spanwise turbulent intensity plotted at top-middle elevation (z = 0.232 m).

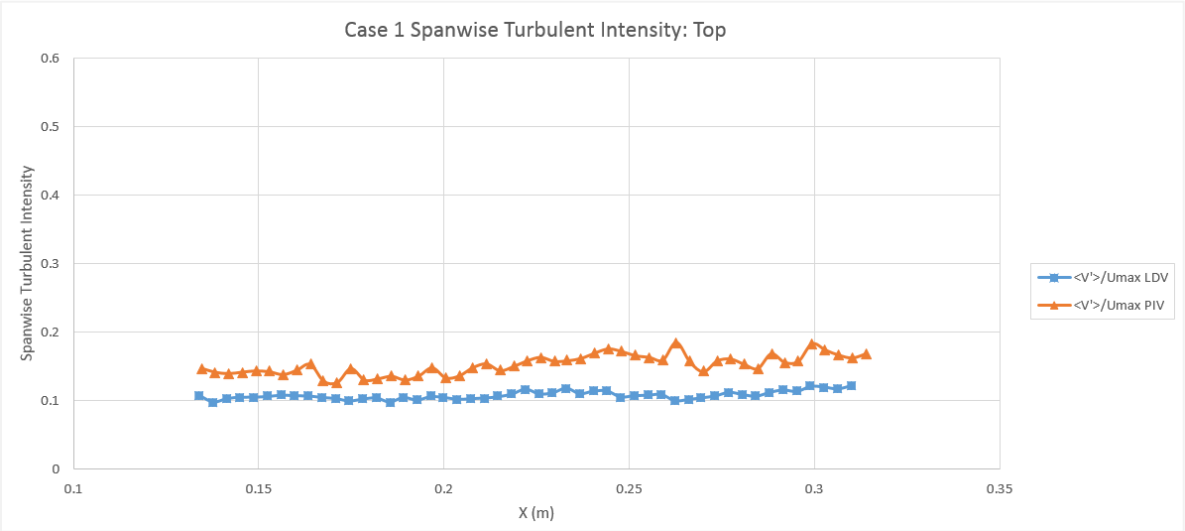

Figure 57. Case 1 – PIV vs LDV average spanwise turbulent intensity plotted at top elevation (z = 0.331 m).

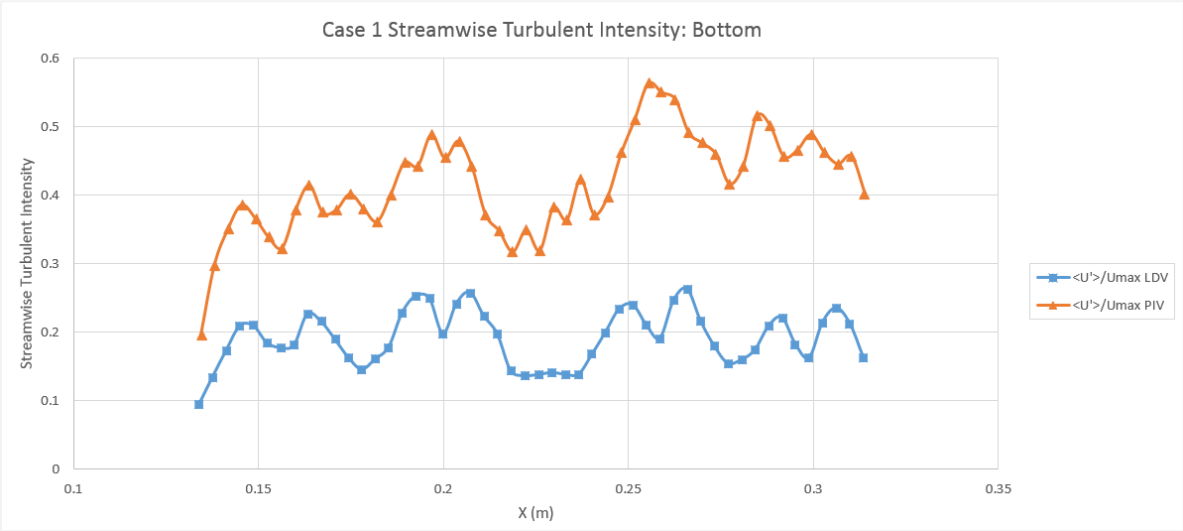

Figure 58. Case 1 – PIV vs LDV average streamwise turbulent intensity plotted at bottom elevation (z = 0.091 m).

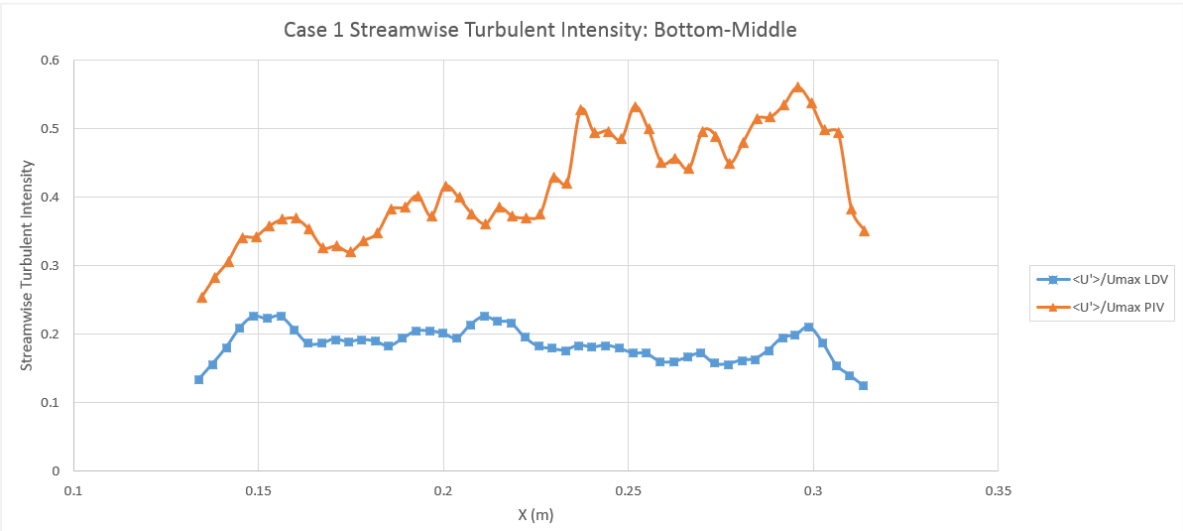

Figure 59. Case 1 – PIV vs LDV average streamwise turbulent intensity plotted at bottom-middle elevation (z = 0.162 m).

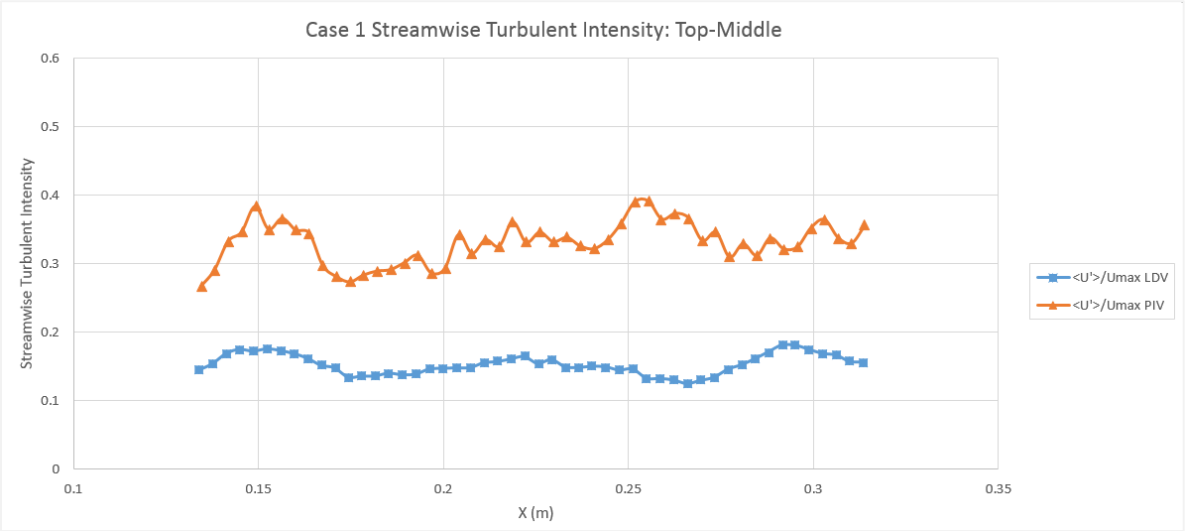

Figure 60. Case 1 – PIV vs LDV average streamwise turbulent intensity plotted at top-middle elevation (z = 0.232 m).

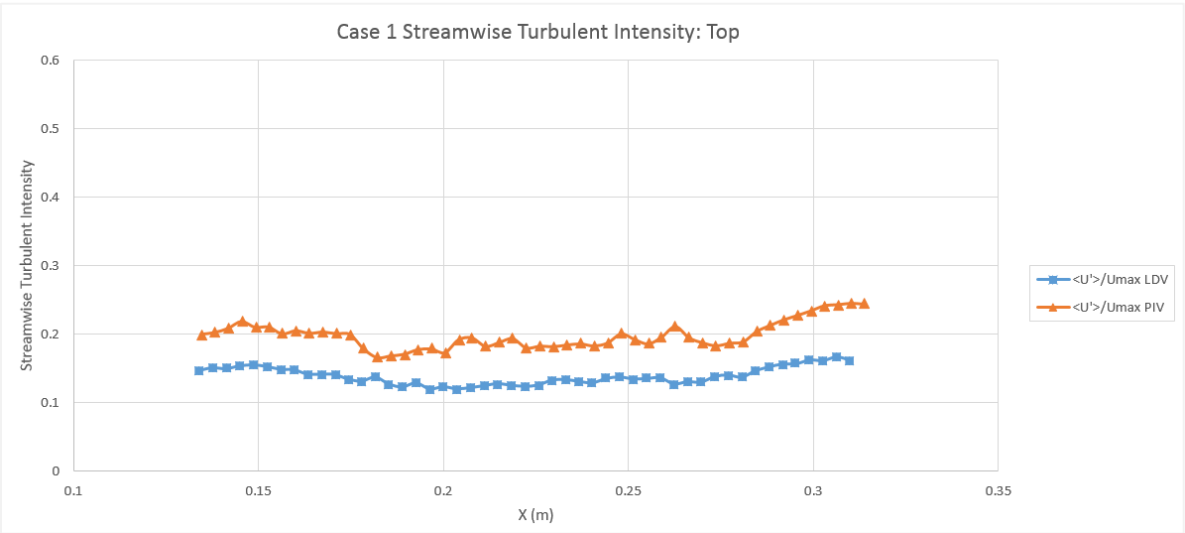

Figure 61. Case 1 – PIV vs LDV average streamwise turbulent intensity plotted at top elevation (z = 0.331 m).

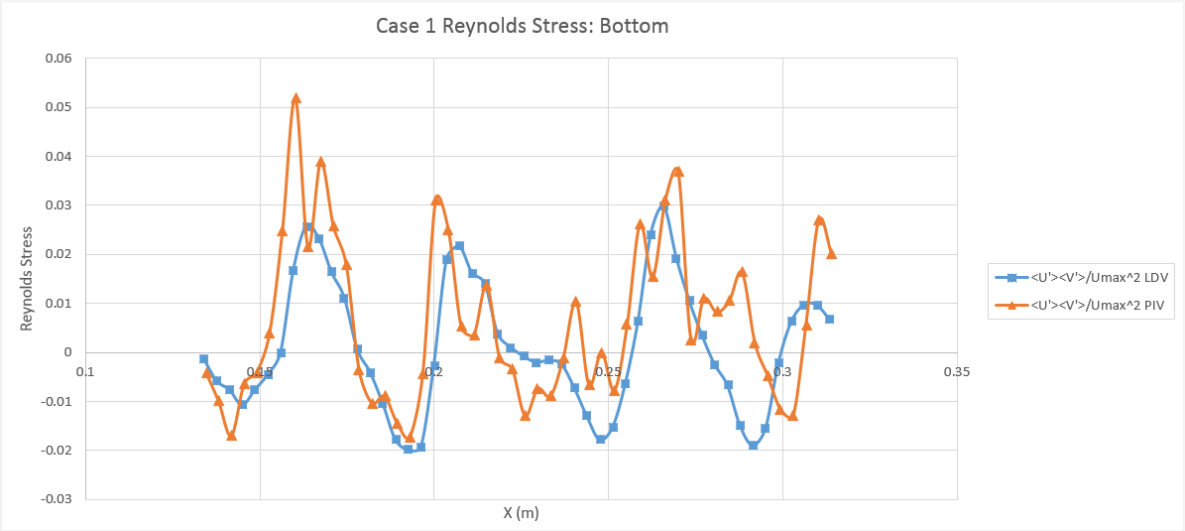

Figure 62. Case 1 – PIV vs LDV average Reynolds stress plotted at bottom elevation (z = 0.091 m).

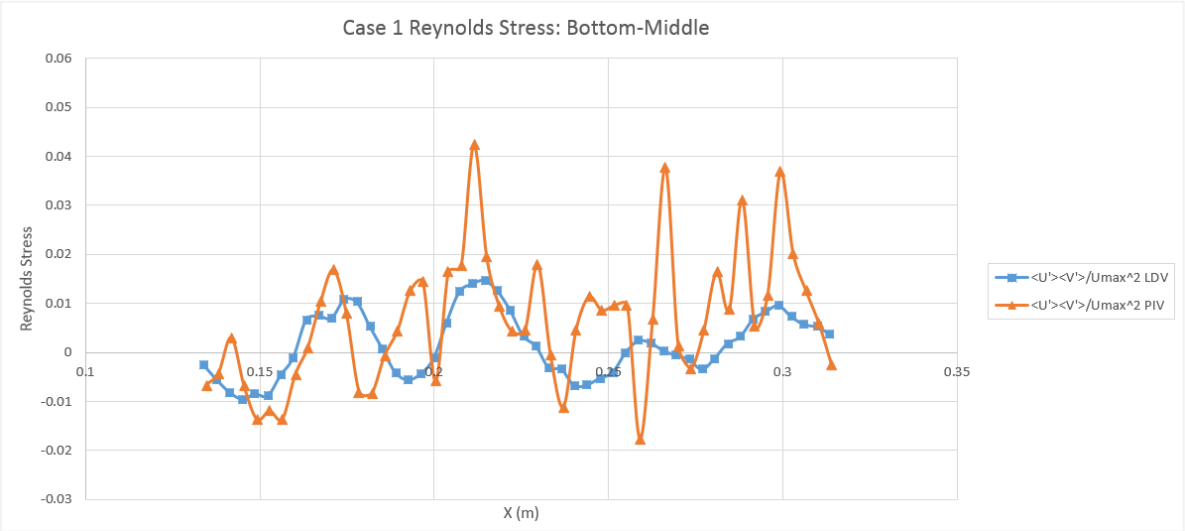

Figure 63. Case 1 – PIV vs LDV average Reynolds stress plotted at bottom-middle elevation (z = 0.162 m).

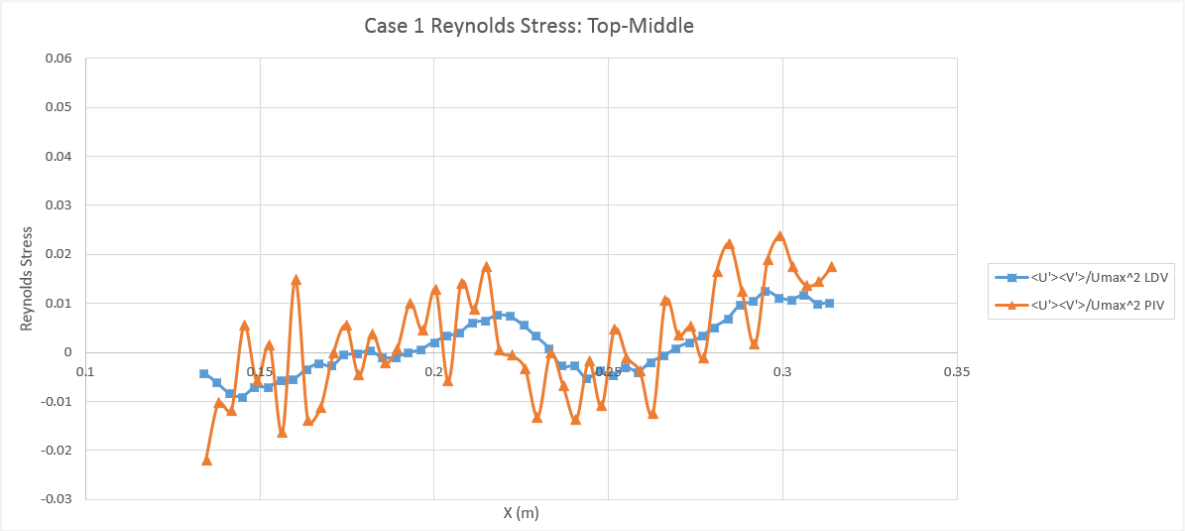

Figure 64. Case 1 – PIV vs LDV average Reynolds stress plotted at top-middle elevation (z = 0.232 m).

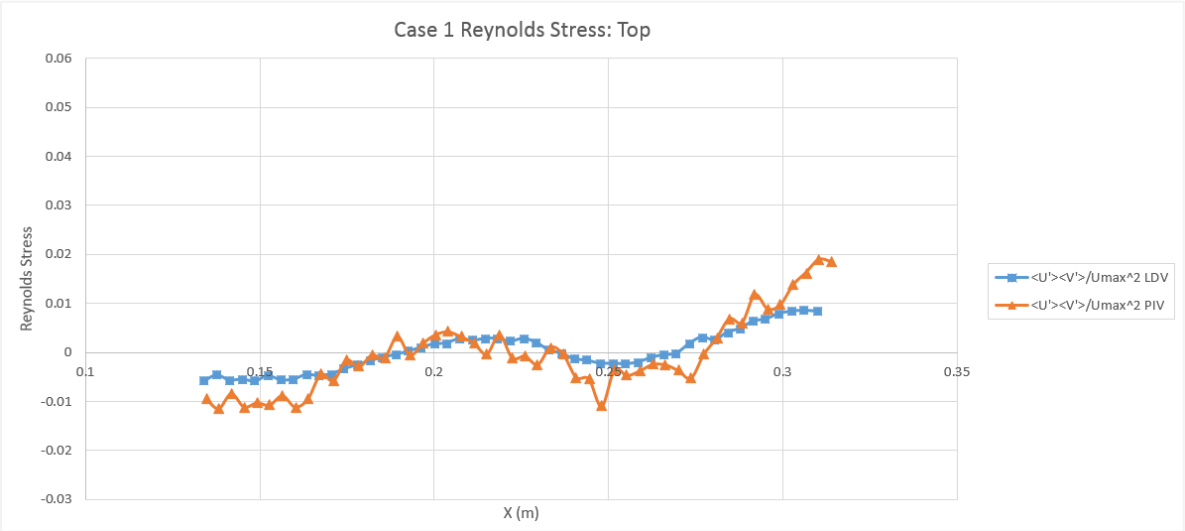

Figure 65. Case 1 – PIV vs LDV average Reynolds stress plotted at top elevation (z = 0.331 m).

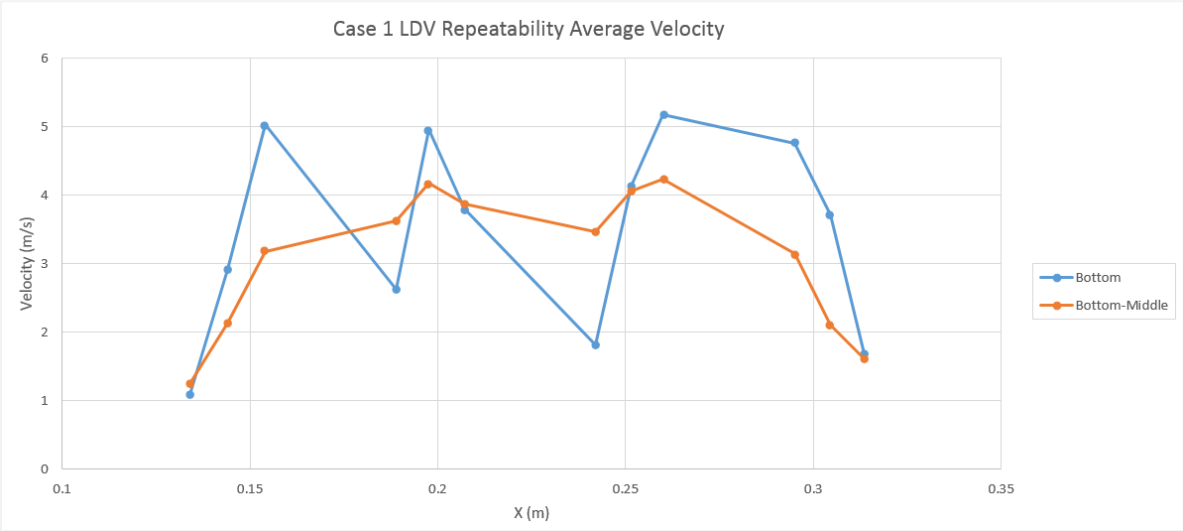

Figure 66. Case 1 – LDV repeatability average velocity for bottom and bottom-middle elevations (z = 0.091 m and z = 0.162 m, respectively).

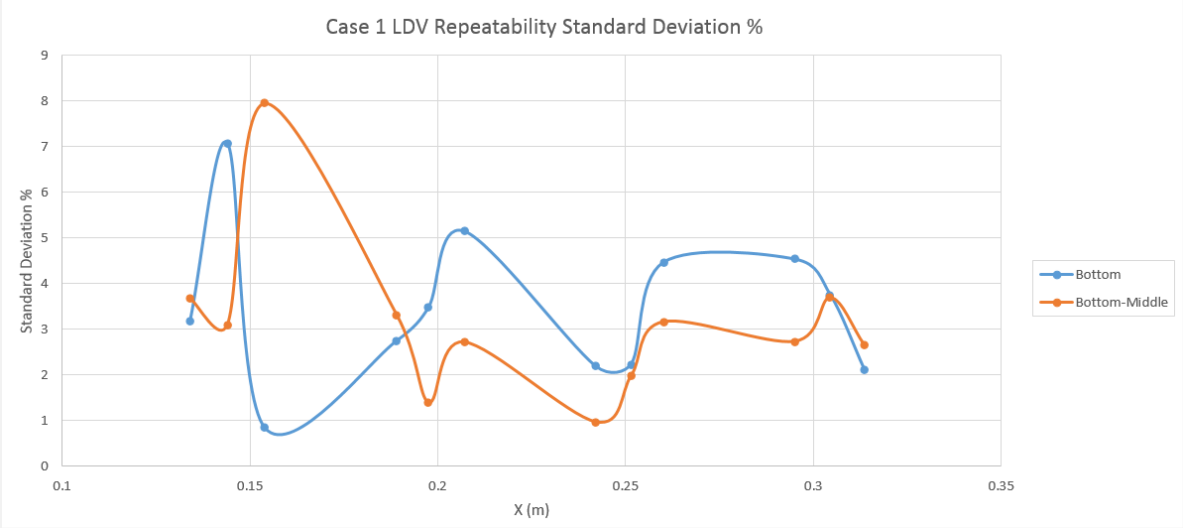

Figure 67. Case 1 – LDV repeatability standard deviation percentage for bottom and bottom-middle elevations (z = 0.091 m and z = 0.162 m, respectively).

Before beginning the general discussion on the data, there are a couple of differences between the PIV and LDV techniques that should be noted, which serve to provide an improved understanding of both data sets and aid in their analyses. First, as stated before, the number of samples per each data point for the PIV and LDV data sets are different by an order of magnitude, with LDV having 1500 samples and PIV having 150 samples. This can help to explain some discrepancies between the plots, in which the PIV data appears to have more fluctuations between adjacent data points than the LDV data, which usually appears to be much smoother. Second, the velocity gradients in the upper plenum tend to decrease with increasing height, which are significantly smaller at the top elevation than at the bottom elevation. It is reported that PIV is known to underperform on regions with high velocity gradients (Hart, 1999). It is suspected that many of the plots for PIV do not match closely with the LDV for this reason. Third, the amount of time it took to collect the PIV data was on the order of an hour, whereas the total acquisition time for the LDV experiments was 18 hours on average. While long-term transient phenomena cannot be entirely ruled out, the LDV data would likely exhibit peculiarities due to any hypothetical transients. These observations are not indictments on the PIV data, nor should they be misconstrued to mean the LDV data is better or more accurate. They are merely factors in explaining some of the discrepancies between each. As a side note, the maximum standard errors related to both techniques were calculated and are featured in Table 8. It is shown that both techniques exhibit a relatively small amount of statistical error, with PIV having no more than 5% standard error and LDV having no more than 1% standard error.

Table 8. Maximum normalized standard error percentage for both measurement techniques.

Maximum Standard Error		
	Case 1a	Case 1
PIV (%)	4.74	4.05
LDV (%)	0.78	0.68

For Case 1a, the comparison between the velocity profiles of LDV and PIV tends to vary by elevation. The bottom elevation shows excellent matching, aside from the PIV profile appearing to be slightly more spread out than the LDV profile. The bottom-middle elevation exhibits good agreement, though again the PIV is more spread out than the PIV. At this level, jets 1 and 2 have not merged together to the extent that jets 3 and 4 have. The top-middle elevation shows good agreement on the left half of the plot, though the right half is not quite so good. This is odd considering how well PIV and LDV match at the lower elevations. It should also be noted that jets 1 and 2 have merged at this elevation for both techniques. Finally, the top elevation shows poor agreement as compared to the other plots. While it is unclear as to the cause of this discrepancy, the general jet behavior for each technique is similar. However, PIV is skewed with much higher velocities on the right than on the left, as compared to LDV which shows a more even distribution. This is somewhat strange, considering that at the previous elevation both PIV and LDV are skewed with higher velocities towards the right. In this instance, PIV appears to make more physical sense. As a side note, the ninth data point from the right for LDV is

undoubtedly an outlier. There are several plots for LDV, particular for the spanwise turbulent intensities, which also contain suspected outliers.

The turbulent statistics for Case 1a are a mixed bag, so to speak. There are instances of excellent agreement, and instances of very poor agreement. Starting with the spanwise turbulent intensities, the bottom elevation shows fair agreement, with LDV having a more pronounced shape than PIV. The bottom-middle elevation has practically no agreement, with LDV showing considerable fluctuations between adjacent data points on the left side and PIV being much higher in magnitude. The top-middle elevation exhibits much better agreement, though LDV still contains fluctuations on the left side. The top elevation has the best agreement the spanwise turbulent intensities, with both plots being almost identical. Aside from the bottom-middle elevation, the agreement for spanwise turbulent intensities tends to improve with height. This could be attributed to decreasing velocity gradients as the elevation increases, which is also indicated by the magnitude of the turbulent intensities.

As for the streamwise turbulent intensities, there are some striking similarities with the spanwise turbulent intensities. The bottom elevation shows fair agreement, with both PIV and LDV having very similar shapes but PIV having a higher magnitude. The bottom-middle elevation is similar to the bottom in terms of the shape for each technique, though the difference of magnitudes appears to have increased. The top-middle elevation has good agreement, and the top elevation shows the best agreement. Again, agreement between the techniques tends to improve with height, likely due to decreased velocity gradients with

increased elevations. As a side note, the ninth data point for the top elevation is the same data point from the average velocity graph.

The Reynolds stresses show a level of agreement similar to the average velocities. Starting with the bottom elevation, the shapes between PIV and LDV are somewhat similar, with the left side showing much more agreement than the right side. The bottom-middle elevation shows a degree of agreement, though the PIV appears to have small fluctuations between adjacent points. The top two elevations show similar levels of agreement, with the top elevation being much smoother. As with both the streamwise and spanwise turbulent intensities, the agreement between LDV and PIV tends to improve with height. In addition, the fluctuation between data points also tends to smooth out with increasing elevation, with much more drastic changes for PIV than LDV. This could be an effect of the low number of samples for PIV compared with LDV. Since the velocity gradient decreases with elevation, the number of samples needed to for obtaining good turbulent statistics should decrease. This means for the same number of samples at each elevation, the quality of the data should improve with increasing elevation, which is certainly seen in the Reynolds stress plots.

Generally speaking, the agreement between PIV and LDV is fair to excellent in the adiabatic case. However, for the heated case there is generally much less agreement, in part due to LDV and PIV having somewhat dissimilar experimental conditions. This is shown for the average velocity at the bottom elevation, in which the jet 3 for PIV has significantly lower velocity than LDV. In addition, the velocity for the jet 1 for PIV is higher than LDV, though this difference is less severe than jet 3.

The comparisons of the velocity profiles for Case 1 are poor to fair at best. Starting with the bottom elevation, the jets above 1 and 3 do not match well between PIV and LDV. This is likely due to non-uniform boundary conditions for either or both of the experiments, which are rigorously checked before the start of each experiment. At the bottom-middle elevation there is a fair amount of agreement for PIV and LDV, which is surprising given the previous elevation's lack thereof. The top-middle elevation shows a poor level of agreement, and for PIV appears to not make much sense. For PIV, the right side of the plot shows a peak velocity of approximately $0.95u_{max}$. This is much higher than the peak of the bottom-middle elevation and is approximately the same as the peak of jet above riser 4 for the bottom elevation. In contrast, the LDV shows that between the bottom-middle and top-middle elevations, there is no significant increase of velocity on the right side. In this instance the LDV appears to be more physically valid. The top elevation also shows poor agreement, with PIV having a peak velocity of approximately $0.85u_{max}$. This peak velocity is still higher than the bottom-middle elevation, whereas the velocities for LDV tend to decay with height. It is unclear as to why these discrepancies exist at these particular elevations.

There are several contrasts for the spanwise turbulent intensities. The bottom elevation shows that the magnitude for PIV is significantly higher than LDV. This difference is even more pronounced at the bottom-middle elevation, with PIV for both plots being skewed higher towards the right side. The top-middle elevation shows more agreement for LDV and PIV, though there is still a significant gap between the magnitudes. At the top there is a fair amount of agreement for both the shape and

magnitude of both techniques. It should be noted for LDV that all elevations exhibit noticeable levels of symmetry, which is expected given the symmetry of the boundary conditions for LDV.

The streamwise turbulent intensities for Case 1 show some surprising similarities between themselves and the spanwise turbulent intensities. At the bottom elevation there is a large disparity between PIV and LDV. This is seen at the bottom-middle elevation and even the top-middle elevation. Interestingly though, PIV for the first two elevations is skewed with higher values towards the right, while LDV exhibits symmetry and smoothness which is similar to the spanwise turbulent intensities. Finally, at the top elevation there is fair agreement between the techniques, which is also seen in the spanwise turbulent intensities. These similarities between the both components of the turbulent intensities have led to speculation that the skew of PIV at the lower elevations is due to the difference of boundary conditions for the techniques.

The Reynolds stresses for Case 1 are the somewhat agree between each technique, though the PIV appears to fluctuate significantly between adjacent data points. The bottom elevation shows poor agreement between techniques, with PIV exhibiting sporadic fluctuations throughout. Worse still, bottom-middle elevation shows wide fluctuations for PIV which has almost no similarly to LDV. These fluctuations begin to dampen at the higher elevations, with the top-middle showing fair agreement and top showing good agreement. For all elevations, PIV tends to very roughly follow the shape of LDV, though PIV doesn't have a well-defined shape in any of these instances. By contrast, LDV at all elevations appears to be smooth and has definite shape. From the graphs, it appears PIV

does not have a sufficient number of samples to plot the Reynolds stresses except at the higher elevations.

With the analysis for each case discussed, comparison between the adiabatic and heat case is required. Since the boundary conditions for Case 1 are not uniform, it is somewhat difficult to do comparisons. It can be said that in general, the agreement between the techniques was markedly better for the adiabatic case than the heated case, likely due to the difference in agreement between boundary conditions. In addition, the amount of fluctuations between adjacent data points for the PIV plots is more pronounced for the heated case than the adiabatic case. Both of these observations are likely due to the addition of thermal mixing for the heated case, the mechanism for which is not present under adiabatic conditions. This thermal mixing would require additional samples to properly resolve the average velocity and turbulent statistics. These additional samples were not provided in the heated PIV experiment. As a result, in several instances, it seems PIV does not have a sufficient number of samples to resolve the turbulent statistics for the heated condition. This becomes obvious when comparing the Reynolds stress plots for Case 1a and Case 1.

Overall, the average velocities and Reynolds stresses display a degree of agreement. However, both components of the turbulent intensities differed considerable, with PIV overestimating in most cases. This bias is thought to be the result of excessive noise in the PIV data. This noise could have been introduced through certain means. One, for the PIV experiments, it is important to block all ambient light from entering the test section. Even with the considerable means taken to ensure this was not a factor, it is still

possible that background light could have been present. However, a more likely contributor was excessive noise from the laser light itself. The laser used for PIV measurements was a high power, double pulse Beamtech Vlite-200 laser which could supply up to 200 mJ per pulse (Sulaiman, 2015). Though it was used at a much lower intensity than the maximum setting, this still constituted a high intensity output. This output resulted in noticeable amounts of reflections inside of the test section, which were partially filtered out using a background subtraction algorithm in the post-processing of PIV data. These sources of noise are suspected to be primary factors in of PIV overestimating the turbulence intensities, which is present for the vast majority of the plots.

Before beginning the concluding remarks, discussion is needed for the repeatability experiments for both cases. As mentioned before, these experiments were performed to measure the system's stability under steady state conditions and quantify the repeatability of the LDV measurements. The experiments lasted approximately 24 hours and consisted of five repeated runs at two different elevations, bottom and bottom-middle. From this, the average and standard deviation percentage (normalized by each local average velocity) are taken of all five runs. The graphs for the average velocities are not significant, though they were used to normalize the standard deviations. However, the standard deviation percentages are quite important. For both cases, the percentages do not go beyond 10% and rarely go above 5%. For Case 1a, the maximum value is close to 9%, while Case 1 has a maximum value of approximately 8%. Both of these maximum values are on the left side of the plots, on the bottom elevation. It is difficult to whether or not

this has any significance. However, something which should be noted is that at the start-up of every experiment, during the initial calibration of the inlets with the Velocicalc, it is consistently seen that riser 1 fluctuates with a slightly larger range than the other risers. Though these two observations may not be related in the slightest, there is nothing else currently know which would explain this peculiarity. Aside from that, the percentages appear to be low. The bottom elevation for Case 1a had a mean percentage of 2.2%, which is 3.5% for Case 1. The bottom-middle elevation had a mean value 2.7% for Case 1a and is 3.1% for Case 1. From this, it could be inferred that the system behaves quite stably under both conditions, which is easily attributed to the high quality of the system components. It also indicates that the LDV measurements are quite repeatable, both in terms of spatial coordinates and the data quality.

6. CONCLUSIONS

LDV experiments have been conducted to validate the results of the PIV measurements, which have also aided in characterizing the experimental facility by verifying the system's repeatability and performance. Extensive comparisons were made between the PIV and LDV measurements for the streamwise component of normalized velocity, as well as the spanwise and streamwise components of the normalized Reynolds stress and turbulent intensity. Based on these results, several key differences were found between the techniques.

First and foremost, the magnitude of the PIV turbulent statistics did not generally agree well with those of LDV, though in many instances the shapes of each plot had distinct similarities. Also, measurements located at regions of higher elevation tended to have better agreement in magnitude and shape. These higher regions are characterized by velocity gradients significantly smaller than those found at lower elevations. This fact may explain the discrepancies between PIV with LDV, since PIV is known to underperform on regions with high velocity gradients. In addition, it is suspected that the number of samples for PIV, 150 in total, was insufficient for obtaining reasonable statistics. This is compared to LDV, which had 1500 samples per data point.

Second, the comparison between the techniques appear to agree better for the adiabatic case than the heated case. Since the heated case has additional turbulence fluctuations induced by thermal mixing, this may have hindered the PIV measurements. This could also have be due to higher inlet velocities for the heated condition, which result

from the buoyancy of the jets. Higher inlet velocities would lead to higher velocities gradients, which would further inhibit the PIV measurements from obtaining accurate measurements.

Third, relatively speaking the average velocities and Reynolds stresses showed some level of agreement between the techniques. This is in contrast to the turbulence intensities, which were consistently overestimated by PIV. This led to the conclusion that the PIV data contained significantly more noise than the LDV data. Lastly, a lack of symmetric boundary conditions for the heated case was found for the PIV data. This lack of symmetry gave rise to a peculiar phenomenon, in which the magnitude of average velocity at the top-middle and top elevations was significantly higher than that of the bottom-middle elevation. This may have also had an effect on the turbulent statistics, which could aid in explaining the difference between the PIV and LDV turbulent intensities.

Aside from the comparisons between the two techniques, the LDV measurements were found to exhibit a high level of repeatability over the course of 24 hours. Throughout all the measurements for both cases, the standard deviation percentage was found to be no more than 10%, which indicates that the system is highly stable under the steady-state conditions. This is owed largely to the superior quality of the components of the facility.

7. FUTURE WORK

Since only two experimental conditions were explored in this work, the LDV test matrix be expanded to include more cases. In particular, cases involving the reverse flow phenomenon should be prioritized, as they should lead to a better understanding of the behavior of the steady-state behavior of the system under these conditions.

In addition, a strong recommendation calls for some of the PIV experiments to be repeated. When repeating these experiments, there are two manners in which the experiments could be improved: 1) Run the experiments to obtain a greater number of statistics, and 2) use a lower power laser which will minimize reflections inside the upper plenum. By addressing these issues, the new experimental data would likely show more agreement between it and LDV data. If these improvements do not resolve the general differences, higher numbers of samples for both techniques may be needed. There may also exist inherit bias errors in either technique, which could also be investigated.

REFERENCES

Albrecht, H., Damaschke, N., Borys, M., Tropea, C., “Laser Doppler and Phase Doppler Measurement Techniques”, Berlin: Springer (2003).

U.S. DOE Nuclear Energy Research Advisory Committee (NERAC) and the Generation IV International Forum, “A Technology Roadmap for Generation IV Nuclear Energy Systems”, GIF-002-00, https://www.gen-4.org/gif/upload/docs/application/pdf/2013-09/genivroadmap2002.pdf (2002).

Ball, S., “Sensitivity Studies of Modular High-Temperature Gas-Cooled Reactor Postulated Accidents”, Nuclear Engineering and Design 236.5-6, http://www.sciencedirect.com/science/article/pii/S0029549306000379 (2005).

Chapin, D., Kiffer, S., and Nestell, J., “The Very High Temperature Reactor: A Technical Summary”, MPR Associates, Inc., http://www.mpr.com/uploads/news/very-high-temperature-reactor.pdf (2004).

Corradini, M.H., Feltus, M., and Wei, T., “Experimental Studies of NGNP Reactor Cavity Cooling System with Water”, Nuclear Energy University Programs, US Department of Energy, https://neup.inl.gov/SiteAssets/Final%20%20Reports/NEUP_Project_No_09-781_Final_Report.pdf (2012).

Dantec Dynamics, “LDA and PDA Reference Manual”, Skovlunde, Denmark (2011).

Durst, F., Melling, A., & Whitelaw, J., “Principles and Practice of Laser-Doppler Anemometry”, London: Academic Press (1981).

Office of Advanced Nuclear Research, DOE Office of Nuclear Energy, Science, and Technology, U.S. DOE, “Generation IV Nuclear Energy Systems: Ten Year Program Plan,

March 2005", http://nuclear.inl.gov/deliverables/docs/gen-iv-10-yr-program-plan.pdf (2005).

Hart, D., "PIV Error Correction" Springer, Experiments in Fluids 29.1, http://link.springer.com/article/10.1007%2Fs003480050421 (1999).

Konefal, J., et al, "Evaluation of High Temperature Reactors for Potential Application to Thermal In-situ Recovery of Oil Sand", MPR Associates Inc., MPR-3254 Rev. 0, www.ptac.org/attachments/1286/download (2009).

Park, G.H., Cho, Y.J. and Cho, H.K., "Assessment of a New Design for a Reactor Cavity Cooling System in a Very High Temperature Gas-Cooled Reactor", Nuc. Eng. and Tech. 38.1, (2006).

"Preliminary Safety Information Document for the Standard MHTGR," HTGR-86-024, Vol. 1, Amendment 13, U.S. Department of Energy (1992).

Sulaiman, S., "Experimental Investigations of Flow Behavior Inside the Upper Plenum of TAMU Air-Cooled Reactor Cavity Cooling System" (unpublished doctoral dissertation), Texas A&M University, College Station, TX (2015).

Sulaiman, S., Dominguez-Ontiveros, E., Alhashimi, T., Budd, J., Matos, M., & Hassan, Y., "Design Considerations and Experimental Observations for the TAMU Air-Cooled Reactor Cavity Cooling System for the VHTR", AIP Conf. Proc. 1659, 030002 (2015).

TSI, Inc., "Six-Jet Atomizer Model 9306 – Owner's Manual", P/N 1990143, Revision L, Shoreview, MN (2014).

TSI, Inc., "VelociCalc® Air Velocity Meter Model 9545/9545-A", Shoreview, MN: Author (2013).

Tzanos, C.P. and Farmer, M., "Feasibility Study for Use of the Natural Convection Shutdown Heat Removal Test Facility NSTF for Initial VHTR Water-Cooled RCCS Shutdown", ANL-GenIV-079, Nuclear Engineering Division, Argonne National Laboratory, http://www.ipd.anl.gov/anlpubs/2007/08/59753.pdf (2006).

Yeh, Y. and Cummins, H., "Localized Fluid Flows Measurements with He-Ne Laser Spectrometer", Applied Physics Letters, 4, 176-178 (1964).

Zhang, Z., "LDA Application Methods: Laser Doppler Anemometry for Fluid Dynamics". Berlin: Springer (2010).